LBNL–41123/CBP Note–246/PEP-II AP Note AP 97.27

The Electron-Cloud Instability in the Arcs of the PEP-II Positron Ring*

Miguel A. Furman and Glen R. Lambertson

Center for Beam Physics, MS 71-259
Accelerator and Fusion Research Division
Lawrence Berkeley National Laboratory, University of California
Berkeley, CA 94720

March 16, 1998

Abstract

We have applied our simulation code "POSINST" to evaluate, in linear approximation, the contribution to the growth rate of the electron-cloud instability (ECI) from the pumping sections and the dipole bending magnets in the arcs of the PEP-II positron ring. A key ingredient in our model is a detailed description of the secondary emission process off the TiN-coated chambers. Another important element is the analytic computation of the electric field produced by the beam, including the effects from surface charges. Space-charge forces of the electron cloud upon itself are also included, although these forces are negligible under nominal conditions. Bunch-length effects are optionally included by slicing the bunch into several kicks. We conclude that the growth rate is dominated by the pumping sections and scales linearly with the photoelectric yield Y'. For $Y' = 1$, our present estimate is in the range $\sim 1000 - 1300$ s^{-1}, depending upon the value of the photon reflectivity R. This is in the range controllable by the transverse feedback system. The contributions to the growth rate from other magnets and from other sections of the ring remain to be evaluated.

1 Introduction.

It is becoming increasingly clear that the ECI, first identified by Izawa *et al.* [1] at the Photon Factory, can have serious detrimental effects for other positively-charged, high-current, multibunch beams [2]. Over the past two years we have developed a simulation code along the same lines as Ohmi's original work [3], and we have applied it to study the ECI in the pumping sections and dipole bending magnets in the arcs of the PEP-II low-energy (positron) ring [4]. In this article we report further details and minor updates on our previously published results [5].

In our simulation model the electron secondary emission process is described in a fair amount of detail, and the secondary emission yield (SEY) is represented by a fit to experimental measurements of TiN-coated vacuum chamber samples carried out at SLAC [6]. These measurements show a peak SEY $\hat{\delta}_t = 1.066$, which we have adopted for our simulations. This value is achieved after a dose of 10^{18} electrons/cm^2; in the actual operation of PEP-II, such dose will be achieved after $\sim$ 18 A-h of integrated beam charge, which should obtain within the first few weeks of commissioning.

In addition to the SEY, two other basic inputs to the simulation are the photoelectric quantum efficiency Y' and the photon reflectivity R, for which we do not have good data at present. Thus we have set $Y' = 1$ and have estimated the instability growth rate in the two limits, $R \sim 0$ and $R \sim 1$. For $R \sim 1$ our present estimate for the growth rate from the arcs is ~ 1000 s^{-1}; for $R \sim 0$ the estimate is 1300 s^{-1}. In either case, the growth rate is dominated by the pumping sections. Such growth rates are within the range controllable by the feedback system [7].

PEP-II is in a regime in which the ECI growth rate scales roughly linearly with Y' regardless of the precise value of R. This linear scaling is a direct consequence of the low SEY of the TiN coating and of the existence of an antechamber.

*Work supported by the US Department of Energy under contract no. DE-AC03-76SF00098. To be published in the proceedings of the MBI-97 Workshop, KEK, Tsukuba, Japan, 15–18 July 1997.

An important ingredient in the simulation is the computation of the electric field produced by the bunches and by the electrons in the cloud. For this purpose we have made the simplifying assumption that the vacuum chamber is a closed ellipse. This approximation allows us to use the analytic expression for the electric field subject to perfect-conductor boundary conditions [8], which fully includes the effects from the induced surface charges.

The code allows to account for bunch-length effects by dividing the bunch into a specified number of slices. For the pumping sections, however, the bunch length has a negligible effect on the growth rate, so that the simple impulse approximation is quite adequate. For the dipole bending magnets, bunch-length effects are important; in this case, however, we use a modified impulse approximation which sensibly represents the bunch slicing.

We use a very simplified model of the PEP-II ring, consisting of 6 identical arcs and 6 identical field-free straight sections. The arcs are made up of 32 dipole bending magnets and 32 field-free pumping sections. Thus the contribution to the growth rate from other magnets in the arcs, such as quadrupoles, remains to be evaluated. In reality, the "straight" sections do have magnetic fields, so their contribution to the growth rate remains to be evaluated as well. In our calculation we obtain the growth rate from the dipole wake function induced by rigid bunches traveling in specified trajectories. Thus our results are expected to be reliable only in the linear (small amplitude) approximation, and do not shed any light on the large-amplitude regime nor on the possible emittance growth of the beam.

2 Vacuum chamber and photoproduction.

For simplicity we assume that the ring is composed of 6 identical arcs and 6 identical straight sections arranged in a perfect 6-fold symmetry. Each arc has 32 dipole bending magnets of length $L_B = 0.45$ m and 32 pumping sections of length $L_{PS} = 7.15$ m, so that the length of a half-cell is $L_{1/2} = 0.45 + 7.15 = 7.6$ m and the length of the arc is $L_A = 32 \times 7.6 = 243.2$ m. Each straight section is $L_{SS} = 123.35$ m long, for a total model ring circumference of 2199.3 m. Figure 1 sketches a portion of an arc.

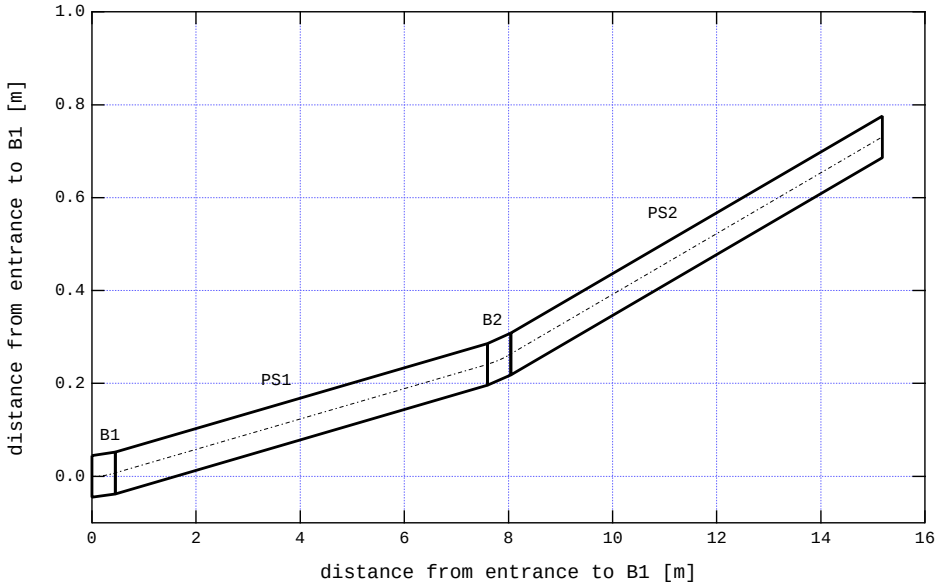

Figure 1: Anamorphic sketch of the plan view of a portion of an arc. B1 and B2 represent two dipole bending magnets, and PS1 and PS2 represent two pumping sections.

2.1 Calculation of the number of photons in the chamber.

The average number of photoelectrons that are generated in a given section of the ring is directly proportional to the average number of photons that strike the vacuum chamber wall of this section. The basic quantity to compute first is the number of photons generated by synchrotron radiation from the passage of *a single bunch* through *a single dipole bending magnet* that strike the vacuum chamber *anywhere* at *any time* after the bunch passage through the magnet. Such quantity is expressed as

$$N_{\gamma/\text{bunch}} = N_{\gamma/p} N_p \tag{2.1}$$

where $N_{\gamma/p}$ is the number of photons radiated per positron and N_p is the number of positrons per bunch.

The beam orbit through a dipole bending magnet has a radius of curvature ρ, and the section of arc subtended by a dipole magnet is $\Delta\theta = 2\pi/192$. The critical energy of the synchrotron radiation from a positron traversing a dipole magnet is given by

$$E_{\text{crit}} = \frac{3\hbar c}{2\rho}\,\gamma^3 \tag{2.2}$$

where γ is the usual relativistic factor of the positron. Each positron generates, on average,

$$N_{\gamma/p} = \frac{5\alpha\gamma}{2\sqrt{3}}\,\Delta\theta \tag{2.3}$$

incoherent photons of all energies and directions upon traversing any given dipole bending magnet ($\alpha \simeq 1/137$ is the fine structure constant). For our purposes, coherent photons can be completely neglected due to their very low energy. Table 1 presents numerical values for the synchrotron radiation from the bending magnets along with other parameters relevant to the ECI simulations.

Table 1: PEP-II synchrotron radiation parameters.

Beam energy, E [GeV]	3.1
Relativistic factor, γ	6066.5
Dipole magnet field, B [Tesla]	0.752
Dipole magnet length, L_B [m]	0.45
Bending radius, ρ [m]	13.75
Dipole magnet arc section, $\Delta\theta$ [mrad]	32.7
Critical energy, E_{crit} [keV]	4.80
No. of radiated photons, $N_{\gamma/p}$	2.09

The number $N_{\gamma/p} = 2.09$ in Table 1 pertains to the radiation emitted at any energy and angle from a positron. However, an important feature of the vacuum chamber in the arcs is an antechamber on the outboard side, whose entrance is sketched in Fig. 2. The purpose of the antechamber is to allow most of the synchrotron radiation to escape from the portion of the vacuum chamber near the beam.

At the present stage of our simulation, we completely neglect all photons that go out the slot leading to the antechamber. Of those photons that are radiated at sufficiently large opening angle that they remain inside the chamber, only those whose energy is larger than the work function of the metal can yield photoelectrons. Therefore, in order to calculate the number of photons that is relevant to our problem, we must integrate the fundamental spectrum of synchrotron radiation [9],

$$\frac{dN_{\gamma/p}}{dn d\phi d\psi} = \frac{\alpha}{3\pi^2} n(\gamma^{-2} + \psi^2)^2 \left[K^2_{2/3}(\xi) + \frac{\psi^2}{\gamma^{-2} + \psi^2} K^2_{1/3}(\xi)\right] \tag{2.4}$$

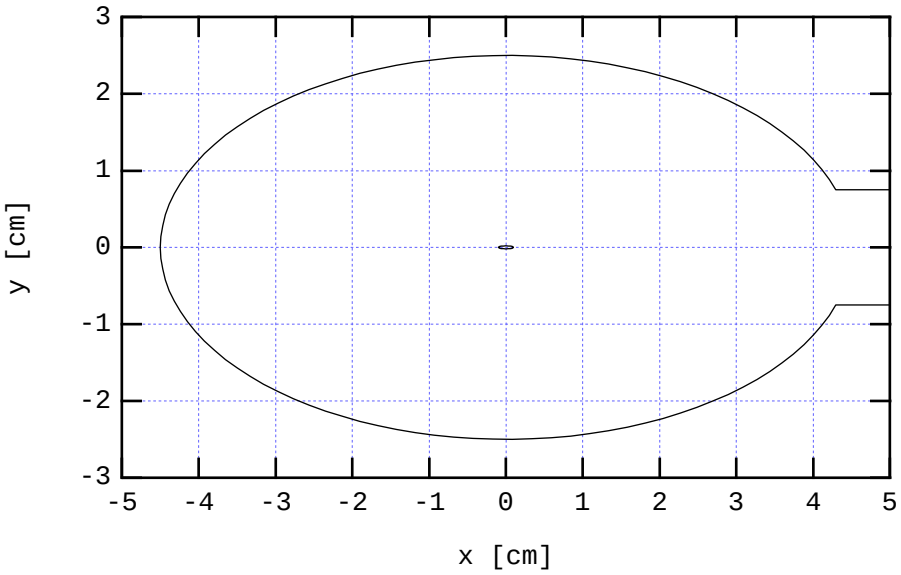

Figure 2: Sketch of the vacuum chamber cross-section and the 1-σ beam ellipse. The chamber is of elliptical shape with semi-axes $a = 4.5$ cm, $b = 2.5$ cm, and the antechamber slot has full height $h = 1.5$ cm.

over the phase space available to the photons. This formula represents the number of photons radiated into a fan of out-of-plane opening angle $d\psi$ when a positron (or any point charge e) moves at constant angular speed ω_0 with relativistic factor $\gamma \gg 1$ through an arc of circle $d\phi$. The $K_\nu(\xi)$'s are modified Bessel functions, and n is the harmonic number of the radiation, $n = \omega/\omega_0 = E/\hbar\omega_0$ where E is the photon energy. The parameter ξ is defined by

$$\xi = \frac{n}{3}(\gamma^{-2} + \psi^2)^{3/2} \tag{2.5}$$

The calculation of $N_{\gamma/p}$ is done by numerical integration taking into account the geometry of the chamber and the curvature of the orbit (a first estimate was provided by Heifets [10], along with an analytic approach to the ECI problem). As it turns out, the PEP-II arc chamber geometry implies a convenient simplification achieved by noting that the minimum vertical opening angle available to the photons inside the chamber, $\psi_{\min} = 8.6\times10^{-4}$, is large compared to $1/\gamma = 1.65\times10^{-4}$. Hence it is legitimate to neglect γ^{-2} *vis à vis* ψ^2 in Eqs. 2.4 and 2.5. In addition to folding the spectrum with the available phase space, one should, in principle, fold it with the angular divergence of the beam in order to take into account the fact that the positrons in a given bunch do not travel in exactly the same arc of circle through the bending magnet. However, this folding can be neglected because the average vertical angular spread of the beam, $\sigma'_y = 1.2 \times 10^{-5}$ rad, is small compared to the typical opening angle of the radiation, $1/\gamma$.

Two important results of the integration are the energy spectrum $dN_{\gamma/p}/dE$ of the photons that strike the wall of the vacuum chamber regardless of their location and angle, and the longitudinal distribution $dN_{\gamma/p}/ds$ of the photons upon first striking the wall regardless of their angle and energy (provided it equals or exceeds 5 eV). These distributions are shown in Fig. 3. Upon performing the integral over E in $dN_{\gamma/p}/dE$, or over s in $dN_{\gamma/p}/ds$, we arrive at the total number of photons of all energies $E \geq 5$ eV and all emission angles that strike the chamber walls when a single positron traverses a single bending magnet, $N_{\gamma/p}$, and their average energy, $\bar{E}$,

$$N_{\gamma/p} = 0.021, \qquad \bar{E} = 15.6 \text{ eV} \tag{2.6}$$

Comparing with Table 1, one sees that only $\sim 1\%$ of the radiated photons remain inside the chamber. This fact has an important beneficial effect on the ECI problem, as we shall discuss below.

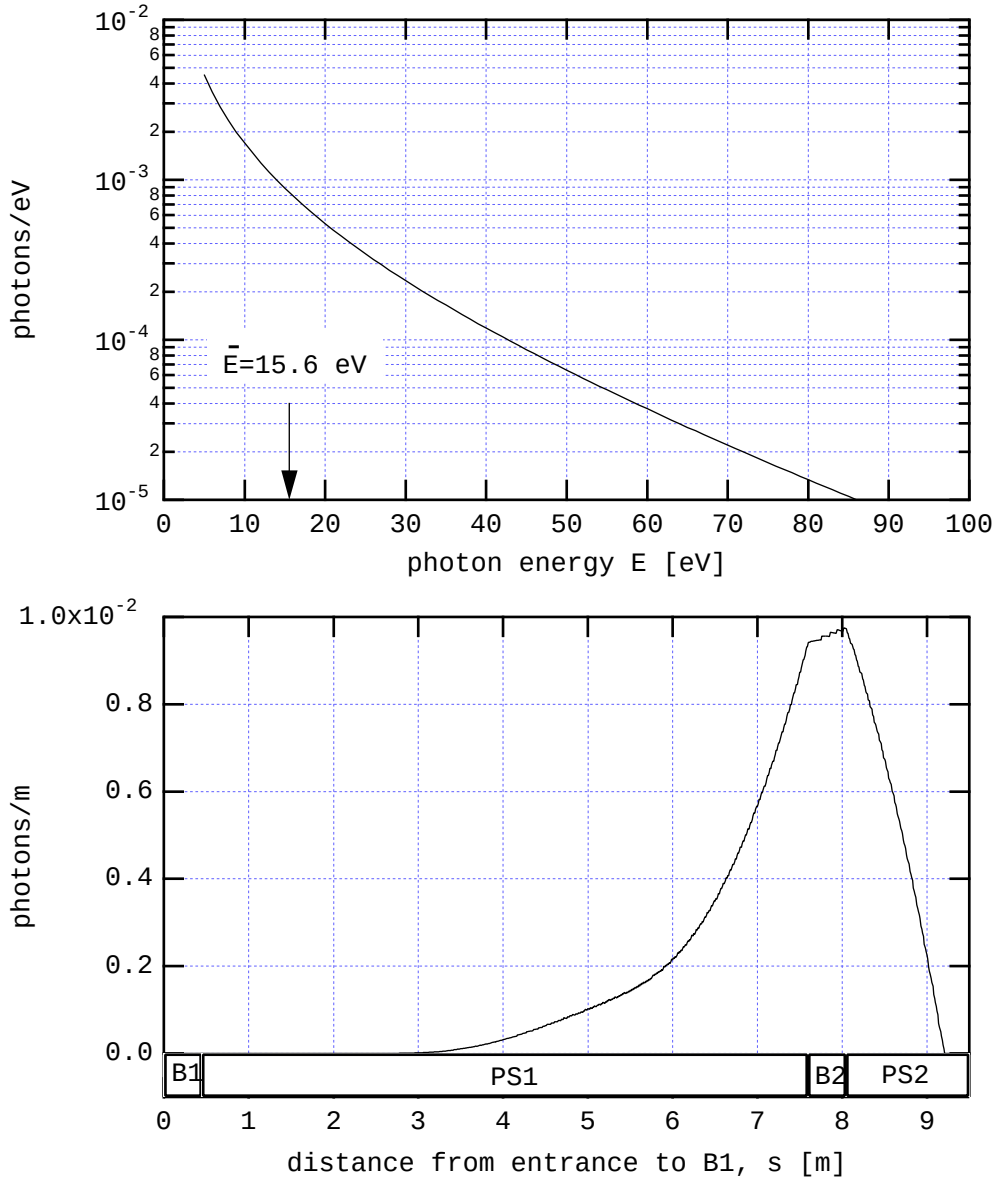

Figure 3: Top: the energy spectrum $dN_{\gamma/p}/dE$ of the photons that hit the vacuum chamber wall that are emitted by a single positron upon traversing a single bending magnet, plotted *vs.* the photon energy E. This spectrum scales as $\sim E^{-2/3}$ at low E, and is exponentially cut off at large E. Bottom: The linear density $dN_{\gamma/p}/ds$ of the "first strike" photons emitted by a single positron traversing bending magnet B1 from left to right. Only photons with energies ≥ 5 eV are counted.

2.2 Definitions of the quantum efficiency.

When a pulse of N_0 photons strikes the surface of a material, a certain number N_r are reflected elastically off the surface and the rest, $N_0 - N_r$, penetrate into the material. Of these, some yield N_e photoelectrons, and the rest, N_a, are absorbed, as sketched in Fig. 4. We define the quantum efficiency Y to be the number

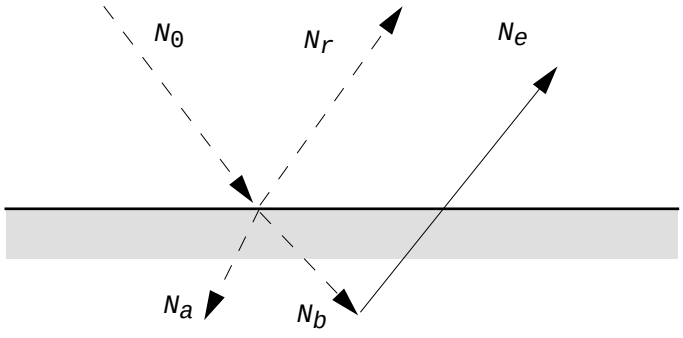

Figure 4: Sketch of the photoelectric effect. Dashed lines represent photons, the solid line photoelectrons.

of photoelectrons generated per incident photon, thus

$$N_e \equiv Y N_0 \tag{2.7}$$

Similarly, we define the reflectivity R and the absorption coefficient A as

$$N_r \equiv R N_0, \qquad N_a \equiv A N_0 \tag{2.8}$$

The basic quantities Y, A and R depend strongly on the type of surface material, photon energy and angle of incidence.

An alternative definition of the quantum efficiency, which is more fundamental and directly relevant to the electron-cloud effect (but less convenient to measure directly), is the number of photoelectrons generated *per photon that penetrated the material*. If we call this Y', then it is given by

$$Y' = \frac{N_e}{N_0 - N_r} = \frac{Y}{1-R} \tag{2.9}$$

This definition is more relevant to the problem at hand because it describes the total number of photoelectrons per photon that are generated anywhere downstream of the photon emission point. To see this, refer to Fig. 5 which sketches the fate of N_0 photons as they bounce inside a chamber. When these photons first strike the wall, they generate YN_0 photoelectrons. A fraction R of the photons is reflected at the surface and strike the wall further downstream, generating an additional RYN_0 photoelectrons. Similarly, a fraction R of these photons is reflected, and hit the chamber walls even further downstream, and so on. Thus the total number of photoelectrons generated is given by

$$N_{e,\mathrm{tot}} = Y N_0 (1 + R + R^2 + R^3 + \cdots) = \frac{Y}{1-R} N_0 = Y' N_0 \tag{2.10}$$

This calculation assumes that fluorescence can be ignored, a good approximation given the low value of the average photon energy $\bar{E}$, and that the reflection process is specular, so that the incident-angle dependence of R and Y is the same for all bounces. In addition, it assumes that all the photons generated by the bunch stay in the vacuum chamber following their creation. In reality, some of the photons will escape to the antechamber before generating photoelectrons, hence $N_{e,\mathrm{tot}}$ given by Eq. (2.10) slightly overestimates their number.

2.3 Calculation of $\bar{N}_e$ for $R \sim 1$.

When a bunch traverses a bending magnet, the synchrotron photons first strike the wall within the first 10 m or so downstream of the magnet, as shown in Fig. 3. However, if the reflectivity is high, $R \sim 1$, most of

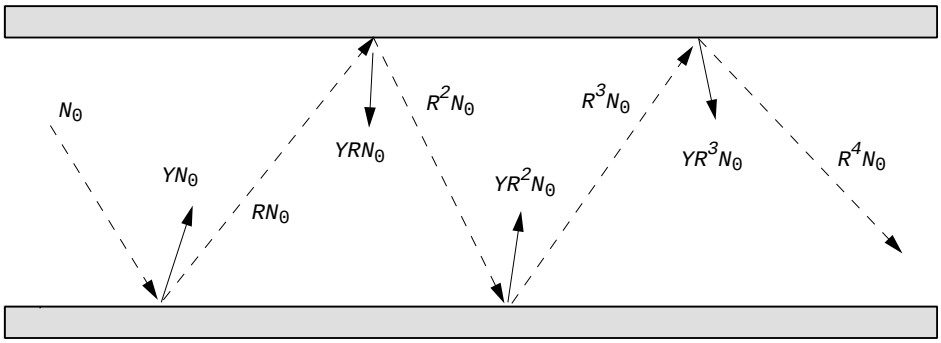

Figure 5: A initial pulse of N_0 photons strikes the wall of a closed vacuum chamber. Upon each bounce, some photoelectrons are generated and some photons are reflected.

these photons will bounce many times before yielding any photoelectrons. Consequently the time-averaged photon distribution is approximately uniform both longitudinally and transversely, and therefore the details of the linear density spectrum in Fig. 3 can be ignored. The time-averaged linear density of photons emitted by a single bunch is therefore $N_{\gamma/\mathrm{bunch}}/L_{1/2}$.

Now let $N_{e/\mathrm{bunch}}$ be the number of photoelectrons generated anywhere in the chamber at any time following the passage of a single bunch through a single dipole bending magnet. According to the discussion in Sec. 2.2, this number is $N_{e/\mathrm{bunch}} = Y' N_{\gamma/\mathrm{bunch}}$. Let us ignore for the moment the straight sections in our model ring. Since the dipole magnets are separated by a distance $L_{1/2}$, the time-averaged number of photoelectrons generated per unit time as a given bunch travels through the ring is

$$\frac{d\bar{N}_e}{dt} = \frac{cN_{e/\mathrm{bunch}}}{L_{1/2}} \tag{2.11}$$

If the ring has circumference C and contains M identical bunches equally spaced by a distance $s_B = C/M$, then the average number of photoelectrons generated per unit time per unit circumferential length from all bunches is

$$\frac{d\bar{N}_e}{dsdt} = \frac{cMY' N_{\gamma/\mathrm{bunch}}}{CL_{1/2}} = \frac{cY' N_{\gamma/\mathrm{bunch}}}{s_B L_{1/2}} \tag{2.12}$$

Thus the average number of photoelectrons generated in a given section of length L during a time equal to a bunch passage, s_B/c, is obtained by multiplying the above average by Ls_B/c,

$$\bar{N}_e = Y' N_{\gamma/\mathrm{bunch}} \frac{L}{L_{1/2}} \tag{2.13}$$

This result is a straightforward consequence of the fact that photons with high reflectivity are uniformly distributed along the length of the chamber with an average linear density $N_{\gamma/\mathrm{bunch}}/L_{1/2}$. As mentioned above, this result applies to a model ring consisting of nothing but arcs. If we now enlarge the model to include straight sections following every arc, the above expression for $\bar{N}_e$ must be diluted by a factor $\mathcal{D}$ to account for the fact that no synchrotron radiation is generated in the straight sections, thus

$$\bar{N}_e = \mathcal{D} Y' N_{\gamma/\mathrm{bunch}} \frac{L}{L_{1/2}} \tag{2.14}$$

Since there is an equal number of arcs and straight sections, clearly this dilution factor must have the value

$$\mathcal{D} = \frac{L_A}{L_A + L_{SS}} \tag{2.15}$$

where L_A and L_{SS} are the lengths of the arc and straight section, respectively. This dilution factor assumes that R is close enough to 1 that the average distance traveled by a photon inside the chamber from generation to conversion is large compared to L_{SS}.

As mentioned earlier, our present model for the ring is simplistic in that it ignores the magnetic fields in the "straight" sections. In the future we shall estimate the contribution from these to the ECI growth, in a more complete model of the ring; this will require a re-evaluation of $\mathcal{D}$.

2.4 Calculation of $\bar{N}_e$ for $R \sim 0$.

If $R \sim 0$ the photons essentially do not bounce in the chamber, and therefore yield photoelectrons (or get absorbed) upon first striking the wall. We must therefore count the photons separately in the dipole magnets and in the pumping straight sections by integrating the linear density $dN_{\gamma/p}/ds$ shown in Fig. 3. Thus we obtain, for the number of photons that hit the chamber wall in a dipole magnet ($N_{\gamma/p,B}$) or in the pumping section ($N_{\gamma/p,PS}$) after being emitted by a single positron traversing a single bending magnet,

$$N_{\gamma/p,B} = 0.43 \times 10^{-2} \tag{2.16a}$$

$$N_{\gamma/p,PS} = 1.67 \times 10^{-2} \tag{2.16b}$$

where $N_{\gamma/p,PS}$ includes the contributions from both PS1 and PS2 in Fig. 3 (note that these two numbers add up to 0.02, as they must).

Therefore, the time-averaged numbers of photoelectrons generated in a dipole bending magnet or in a pumping section in a time interval s_B/c are given by

$$\bar{N}_{e,B} = Y' N_{\gamma/p,B} N_p \tag{2.17a}$$

$$\bar{N}_{e,PS} = Y' N_{\gamma/p,PS} N_p \tag{2.17b}$$

where we have set the dilution factor $\mathcal{D}$ to unity, as it is clear we should when $R \sim 0$.

2.5 Time structure of the photoelectrons.

As mentioned above, the number of photoelectrons $\bar{N}_e$ calculated in Sections 2.4 and 2.3 are time-averaged values. The simulation of the electron-cloud effect, on the other hand, requires the spatial and temporal details of the photoemission process. When the beam traverses a dipole bending magnet, the photons that are generated have the same time structure as the beam. This fact has an important consequence for the beam kick received by the photoelectrons upon being created, as discussed in Sec. 5.4.

3 Electrons produced by ionization.

When a bunch with N_p relativistic charged particles traverses a distance L in a gas of density n it produces a number of ions $N_i = n\sigma N_p L$, where σ is the single-charge ionization cross-section. If we assume that the ions produced are singly-charged, N_i is also the number of ionization electrons. Expressing the density in terms of the pressure and temperature,

$$n\ [\text{molecules/cm}^3] = 9.7 \times 10^9\ \frac{p\ [\text{nTorr}]}{T\ [\text{K}]} \tag{3.1}$$

and assuming room temperature ($T = 294$ K), a pressure $p = 1$ nTorr and a typical cross-section $\sigma = 2$ Mbarns, we obtain

$$N_i = 0.66 \times 10^{-8} N_p L \tag{3.2}$$

where L is in units of m. Comparing Eq. (3.2) with Eqs. (2.16) and (2.17) we see that, for a typical value $Y' = 1$, the number of ionization electrons is ~ 5 orders of magnitude smaller than the number of photoelectrons. Therefore, it is usually safe to ignore ionization electrons in our problem. One should keep in

mind, however, that ionization electrons are produced in the neighborhood of the beam, while photoelectrons are produced on the chamber walls, so this may lead to a significant effect in the electron density distribution in regions with a strong dipole magnetic field if $R \sim 0$. Furthermore, in the parameter regime relevant to PEP-II (and other machines for which the ECI is an issue), $N_{\gamma/p}$ depends more strongly on the beam energy than does N_i, so that ionization electrons may dominate if the beam energy is sufficiently low.

4 Secondary emission process.

An electron with kinetic energy E_0 striking a surface at an angle θ_0 relative to the surface normal yields an average of $\delta_t(E_0, \theta_0)$ electrons. This average is the SEY of the surface. A related quantity is $d\delta_t/dE$, where E is the total kinetic energy of the emitted secondaries. An important parameter of the SEY is the peak value at normal incidence, $\hat{\delta}_t$. A favorable situation *vis à vis* the ECI requires $\hat{\delta}_t$ to be as low as possible. The PEP-II vacuum chambers are made of aluminum, which, if in pure form, has $\hat{\delta}_t \simeq 0.9$, a rather low value. Unfortunately, the surface is normally covered with a layer of Al_2O_3, which has $\hat{\delta}_t \simeq 2$, a very high value. As discussed in more detail below, early simulations showed that, with this value of the SEY, the ECI growth rate would be unacceptably large. As a result, it was decided to coat the chambers with a layer ~ 1000 Å thick of TiN, which has a lower SEY. Figure 6 shows the experimental curves for δ_t for TiN obtained at SLAC as a function of electron bombardment dose. The value $\hat{\delta}_t = 1.066$ is achieved after a dose of 10^{18} e/cm^2, which takes less than one hour with the experimental setup at SLAC [6].

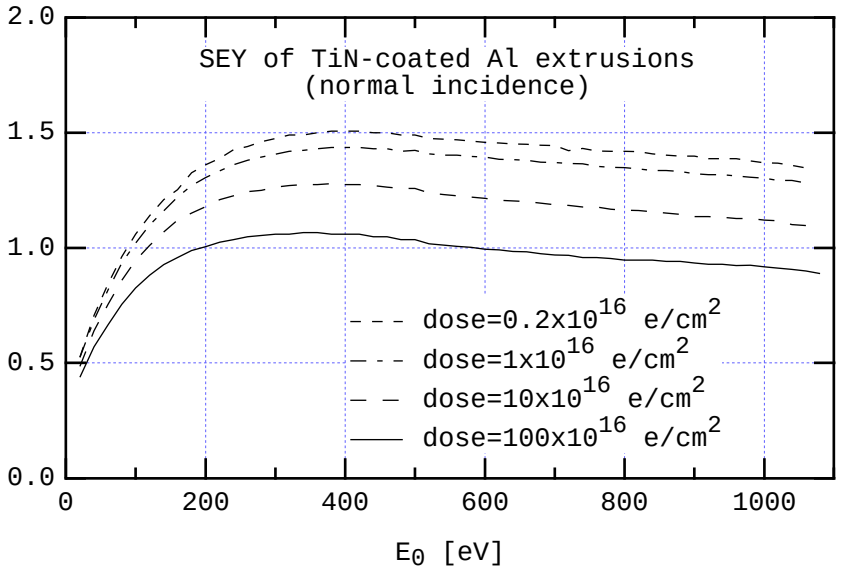

Figure 6: Experimental measurements for the SEY of a sample of TiN-coated aluminum surface at normal incidence. The coating of this particular sample is ~ 2000 Å thick, and the dosing electron energy was 1100 eV [6].

Any reasonable simulation of the secondary emission process requires more detailed information than that provided by $\delta_t(E_0, \theta_0)$ and $d\delta_t/dE$. The reason is that, when the simulated electrons hit the surface, one needs to know, on an event-by-event basis, the number of emitted electrons and their individual energies and directions of emission. The mathematical objects that contain all the information relevant to the process are the "most differential" probabilities

$$\mathcal{P}_n \equiv \frac{dP_n}{dE_1 d\Omega_1 dE_2 d\Omega_2 \cdots dE_n d\Omega_n}, \quad n = 1, 2 \cdots \tag{4.1}$$

for the emission of n electrons. Here E_k and $\Omega_k = (\theta_k, \phi_k)$ are the kinetic energy and solid angle of the k-th ejected electron, respectively. Much is known theoretically and experimentally for many materials about δ_t and, to a lesser extent, about $d\delta_t/dE$. However, to our knowledge, the $\mathcal{P}_n$'s are not known, theoretically or experimentally. Our simulation code POSINST embodies a model for the $\mathcal{P}_n$'s, described below, that is consistent with measured values of δ_t and $d\delta_t/dE$. Obviously such a model is far from unique. We have taken some care to construct the model upon physical principles in order to avoid unphysical results that might not be recognizable in the numerical calculations. The model can be easily updated as more detailed experimental information on the secondary emission process becomes available.

We first note that the probability that n electrons will be emitted with arbitrary energies and directions for a fixed incident angle and energy, $P_n(E_0, \theta_0)$, is obtained by integrating (4.1) over the entire phase space of the secondary electrons,

$$P_n(E_0, \theta_0) = \int (dE)_n (d\Omega)_n \, \mathcal{P}_n \tag{4.2}$$

where the symbols $(dE)_n$ and $(d\Omega)_n$ are the n-body volumes of kinetic energy and solid angle, respectively, $(dE)_n \equiv dE_1 dE_2 \cdots dE_n$ and $(d\Omega)_n \equiv d\Omega_1 d\Omega_2 \cdots d\Omega_n$. The P_n's must obey the conditions

$$P_n \geq 0, \;\; n = 0,\, 1,\, 2,\, \cdots \qquad \text{and} \quad \sum_{n=0}^{\infty} P_n = 1 \tag{4.3}$$

where P_0 is the probability that the incident electron is absorbed without the emission of any electrons. The SEY is the average electron multiplicity in the collision,

$$\delta_t(E_0, \theta_0) = \langle n \rangle \equiv \sum_{n=1}^{\infty} n P_n \tag{4.4}$$

and $d\delta_t/dE$ is given by[1]

$$\frac{d\delta_t}{dE} = \sum_{n=1}^{\infty} n \int (dE)_n (d\Omega)_n \, \mathcal{P}_n \, \delta(E - E_1 - E_2 - \cdots - E_n) \tag{4.5}$$

This equation yields δ_t upon integration over E from 0 to ∞, as it should. Eqs. (4.2–4.5), along with the requirement of energy conservation, provide the basic constraints to construct the model for $\mathcal{P}_n$

4.1 Model of the SEY at normal incidence.

The generally-accepted picture of secondary emission [11] is the following: when a current I_0 of electrons strikes the surface of a material, a certain portion I_e is reflected elastically off the surface, and the rest penetrates into the material. Some of these electrons scatter from one or more atoms and are reflected back out (these are the so-called "rediffused" electrons); we call the corresponding current I_r. The rest of the electrons interact in an inelastic way with the material and yield the so-called "true secondary electrons," whose current we call I_{ts}. We neglect characteristic as well as Auger electrons. Figure 7 sketches the situation.

Referring to Fig. 7, we define the yields for each type of electron by

$$\delta_e = \frac{I_e}{I_0}, \qquad \delta_r = \frac{I_r}{I_0}, \qquad \delta_{ts} = \frac{I_{ts}}{I_0} \tag{4.6}$$

These yields are normalized to the *incident current*. In the literature one often encounters the more fundamental (but less practical) definitions in which the yields are normalized to the *penetration currents*; we shall not deal with these here. The basic quantity used in the simulation program is the total yield δ_t, defined by

$$\delta_t = \frac{I_e + I_r + I_{ts}}{I_0} = \delta_e + \delta_r + \delta_{ts} \tag{4.7}$$

[1] We follow the standard convention of using the symbol δ for the SEY which should not be confused with the delta-function on the right-hand side of this equation.

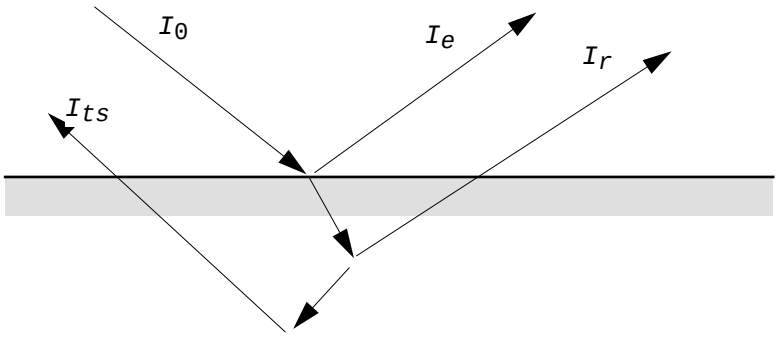

Figure 7: Sketch of the currents that are used to define the different components of secondary emission.

In the following subsections we present our model for incident energy and angle dependence of each of these three components.

4.1.1 True secondary electrons.

The true secondaries dominate the SEY except at low incident energies ($E_0 \lesssim 40$ eV), where the elastic and rediffused components become more important. The energy and angular dependence of δ_{ts} are usually well fit experimentally by a scaling function $D(x)$ [11, 12],

$$\delta_{ts}(E_0, \theta_0) = \hat{\delta}(\theta_0) D(E_0/\hat{E}(\theta_0)) \tag{4.8}$$

so that all dependence on the surface and incident angle θ_0 is contained in $\hat{\delta}$ and $\hat{E}$. The scaling function $D(x)$ is defined so that it satisfies the conditions $D(1) = 1$ and $D'(1) = 0$, which are, of course, chosen to ensure that δ_{ts} reaches a peak value $\hat{\delta}$ at an energy $E_0 = \hat{E}$.

The function $D(x)$ is approximately a universal curve. For our purposes, we have chosen the simplest form that satisfies the above-mentioned conditions and that allows a good fit to the data in Fig 6, namely

$$D(x) = \frac{sx}{s - 1 + x^s} \tag{4.9}$$

where the parameter s must be constrained to be > 1. This function is shown in Fig 8.

The TiN SEY data at normal incidence, shown in Fig. 6, is well fit with $s = 1.44$, $\hat{\delta} = 0.946$ and $\hat{E} = 350$ eV. The data actually has a peak value $\hat{\delta}_t = 1.066$; the difference between 0.946 and 1.066 is made up by the contributions from the elastic and rediffused components. The experimental measurements for incidence away from normal [6] demand that all three parameters $\hat{\delta}$, $\hat{E}$ and s depend on the incident angle θ_0.

4.1.2 Elastically reflected electrons.

As we do not have our own measurements of this component of the SEY, we have roughly fitted data from the literature in the form [13]

$$\delta_e(E_0) = P_{1,e}(\infty) + (\hat{P}_{1,e} - P_{1,e}(\infty)) \exp\left(-(E_0 - E_e)^2/2\Delta^2\right) \tag{4.10}$$

with $P_{1,e}(\infty) = 0.02$, $\hat{P}_{1,e} = 0.1$ and $E_e = \Delta = 5$ eV. The parametrization (4.10) is constructed so that $\delta_e(E_0)$ peaks at $E_0 = E_e$ with a value $\hat{P}_{1,e}$ and has an asymptotic value of $P_{1,e}(\infty)$ at large E_0.

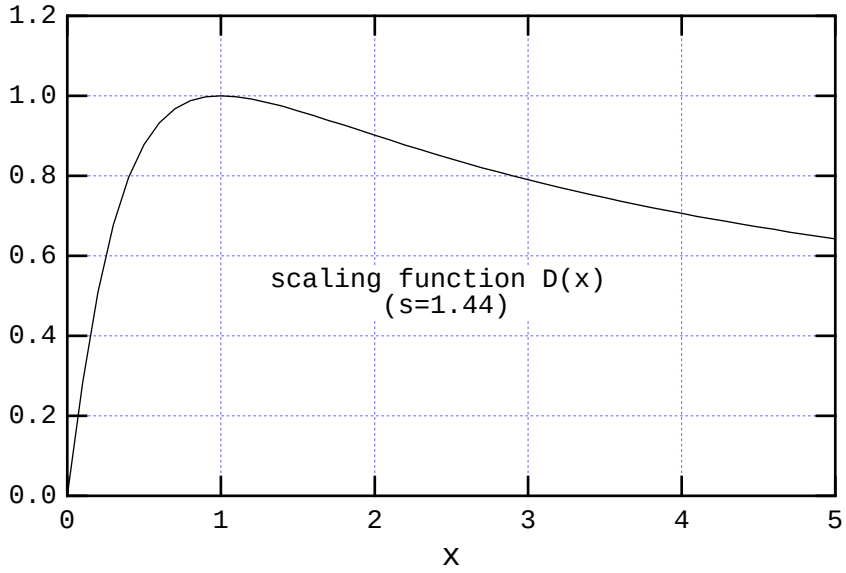

Figure 8: The scaling function $D(x)$, Eq. (4.9), for $s = 1.44$.

4.1.3 Rediffused electrons.

In this case we also have made a rough fit to published data of the form [13]

$$\delta_r(E_0) = P_{1,r}(\infty)\left(1 - \exp(-(E_0/E_r)^2)\right) \tag{4.11}$$

with $P_{1,r}(\infty) = 0.1$ and $E_r = 5$ eV.

4.1.4 Total secondary emission yield.

The parameters listed above are chosen so that, at normal incidence, the total yield has a peak value $\hat{\delta}_t = P_{1,e}(\infty) + P_{1,r}(\infty) + \hat{\delta}_0 = 1.066$ and this peak occurs at an energy $E_0 = \hat{E} = 350$ eV. These are the values that correspond to the data shown in Fig. 6.

4.2 Incident-angle dependence.

For smooth surfaces, the incident-angle dependence of $\hat{\delta}$ and $\hat{E}$ is usually well parametrized by a power law of the form $\hat{\delta}(\theta_0) \propto (\cos\theta_0)^{-a}$ and $\hat{E}(\theta_0) \propto (\cos\theta_0)^{-b}$, where θ_0 is measured relative to the normal to the surface [12]. For technical surfaces, such as the PEP-II vacuum chamber even after TiN coating [6], we have found that these parametrizations are inadequate. A better fit is obtained with

$$s(\theta_0) = s(0) \times (1 - 0.18(1 - \cos\theta_0)) \tag{4.12a}$$

$$\hat{E}(\theta_0) = \hat{E}(0) \times (1 + 0.7(1 - \cos\theta_0)) \tag{4.12b}$$

$$\delta_t(\theta_0) = \delta_t(0) \times (1 + 0.26(1 - \cos^2\theta_0)) \tag{4.12c}$$

The numerical constants appearing in Eq. (4.12), including the powers of $\cos\theta_0$, are only approximate, and in fact were obtained from the incident-angle dependence measurements for an uncoated aluminum sample. More recent data [6] for a TiN-coated sample seem to indicate that some of the numerical constants are different from those above. Nevertheless, our simulations for the ECI for PEP-II show that most electron collisions are near normal incidence, so we do not expect qualitative changes from the results presented here.

4.3 Angular distribution of the emitted electrons.

It is well-known that the true secondary electrons emitted from amorphous surfaces have a $\cos\theta$-distribution in angle, which is fairly independent of the incident angle θ_0. This is not quite true of the elastically reflected and rediffused electrons, which have more complicated angular distributions. However, spot-checks show that the ECI simulation results are fairly insensitive to the angular distribution. Therefore, for simplicity, we choose in our simulation a $\cos\theta$-distribution for all emitted electrons, regardless of the physical mechanism by which they were generated, *i.e.*,

$$\mathcal{P}_n = \frac{dP_n}{(dE)_n} \times \frac{\cos\theta_1 \cos\theta_2 \cdots \cos\theta_n}{\pi^n} \tag{4.13}$$

where the emission angles θ_k are measured relative to the normal to the surface at the collision point. The normalization factor π^{-n} ensures that the integral $\int (d\Omega)_n$ over the hemisphere away from the surface is unity.

4.4 Energy distribution of the emitted electrons.

Next we make the assumption that, for $n \geq 1$, $dP_n/(dE)_n$ is of the form

$$\frac{dP_n}{(dE)_n} = f_n(E_1) f_n(E_2) \cdots f_n(E_n)\, \theta(E_0 - E_1 - E_2 - \cdots - E_n) \tag{4.14}$$

where the f_n's are the single-electron kinetic energy distributions. This expression means that the electrons are emitted almost independently of each other; the only constraint that they must collectively obey, which is enforced by the θ-function, is that their aggregate energy should not exceed the primary electron energy E_0.

The next simplifying assumption consists in treating differently the $n = 1$ case from the others. The purpose of this assumption is to readily obtain from Eq. (4.5) an expression for $d\delta_t/dE$ that resembles the experimental data. Thus we assume that f_1 consists of three components, namely elastic, rediffused and true secondary, while the f_n's for $n \geq 2$ contain only the component from true secondary electrons. Physically, this decomposition means that if an electron is elastically backscattered or rediffused, it will not generate true secondary electrons and conversely, if 2 or more electrons are generated, they all are true secondaries. This decomposition sounds plausible, given the fact that elastic and rediffused electrons dominate the SEY at low incident energies while true secondaries dominate it at high energies. However, we do not have a firm justification; nevertheless, for the purposes of studying the ECI, it probably does not matter very much how the secondary electrons are attributed to different generation mechanisms as long as the basic quantities δ_t and $d\delta_t/dE$ are approximately correct. Thus we set

$$f_1 = f_{1,e} + f_{1,r} + f_{1,ts}, \qquad f_n = f_{n,ts},\ n \geq 2 \tag{4.15}$$

Correspondingly, Eq. (4.14) implies

$$P_1 = P_{1,e} + P_{1,r} + P_{1,ts}, \qquad P_n = P_{n,ts},\ n \geq 2 \tag{4.16}$$

and from Eq. (4.4) we obtain

$$\delta_e = P_{1,e}, \qquad \delta_r = P_{1,r}, \qquad \delta_{ts} = \sum_{n=1}^{\infty} n P_{n,ts} \tag{4.17}$$

The assumed explicit forms for the f_n's are:

$$f_{1,e}(E, E_0, \theta_0) = \delta_e(E_0, \theta_0)\, \frac{2e^{-(E-E_0)^2/2\sigma_e^2}}{\sqrt{2\pi}\sigma_e \operatorname{erf}(E_0/\sqrt{2}\sigma_e)} \tag{4.18a}$$

$$f_{1,r}(E, E_0, \theta_0) = \delta_r(E_0, \theta_0)\, \frac{2E}{E_0^2} \tag{4.18b}$$

$$f_{n,ts}(E, E_0, \theta_0) = F_n(E_0, \theta_0) E^{p-1} e^{-E/\epsilon}, \quad n \geq 1 \tag{4.18c}$$

For our simulations for PEP-II we choose the numerical values $\sigma_e = 2$, $p = 2$ and $\epsilon = 5$ eV.

The above forms for $f_{1,e}$ and $f_{1,r}$ are constructed so that they satisfy Eqs. (4.2) and (4.14) for $n = 1$,

$$P_{1,i} = \int_0^{E_0} dE\, f_{1,i} = \delta_i, \quad i = e, r \tag{4.19}$$

The quantity F_n appearing in $f_{n,ts}$ is related to $P_{n,ts}$ *via* the integral

$$P_{n,ts} = \int_0^{\infty} (dE)_n\, f_{n,ts}(E_1) f_{n,ts}(E_2) \cdots f_{n,ts}(E_n)\, \theta(E_0 - E_1 - E_2 - \cdots - E_n) = \frac{(\epsilon^p \Gamma(p) F_n)^n\, \gamma(np, E_0/\epsilon)}{\Gamma(np)} \tag{4.20}$$

where $\gamma(z, x)$ is the incomplete gamma function [14].

The final ingredient in the definition of the model is the connection between $P_{n,ts}$ and δ_{ts}. For this we assume a simple Poisson distribution,

$$P_{n,ts}(E_0) = \frac{(\delta_{ts})^n}{n!} e^{-\delta_{ts}},\ n \geq 1 \tag{4.21}$$

This distribution has a mean $\langle n \rangle = \delta_{ts}$, as it should in order for δ_{ts} to have the required meaning of being the average number of secondary electrons.

With all ingredients above, it is straightforward to compute $d\delta_t/dE$ from Eq. (4.5); we obtain

$$\frac{d\delta_t}{dE} = \theta(E_0 - E) \left[f_{1,e} + f_{1,r} + \frac{1}{\epsilon} \exp(-\delta_{ts} - E/\epsilon) \sum_{n=1}^{\infty} \frac{(\delta_{ts})^n\, (E/\epsilon)^{np-1}}{(n-1)!\, \gamma(np, E_0/\epsilon)} \right] \tag{4.22}$$

Figure 9 shows plots of $d\delta_t/dE$ that result from the above equation for $E_0 = 50$ and 100 eV. These curves are consistent with measured data.

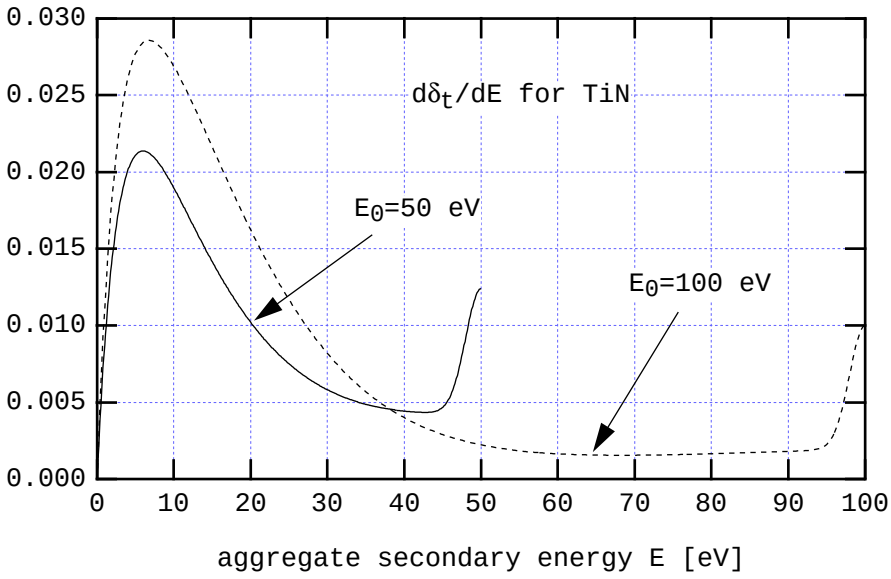

Figure 9: The energy dependence of the SEY, $d\delta_t/dE$, at normal incidence for incident electron energies $E_0 = 50$ and 100 eV. This function is computed for the parameters stated in the text, keeping up to the $n = 10$ term in Eq. (4.22).

4.5 Absorption probability.

The probability P_0 that an incident electron gets absorbed with no electrons generated is determined from Eq. (4.3),

$$P_0 = 1 - \sum_{n=1}^{\infty} P_{n,ts} - P_{1,e} - P_{1,r} = e^{-\delta_{ts}} - \delta_e - \delta_r \tag{4.23}$$

Our model does not guarantee that $P_0 \geq 0$; this condition must be enforced by appropriate parameter choices.

4.6 Algorithm for the secondary emission process.

When an electron hits the chamber wall, the simulation code POSINST uses the SEY model described above in the following sequence of steps:

1. Record the incident energy E_0 and angle θ_0 relative to the normal to the surface.
2. Compute δ_{ts}, δ_e and δ_r according to Eqs. (4.8), (4.10) and (4.11), including the angular dependence factors in Eq. (4.12).
3. Compute the probabilities P_n for $n = 1,\ 2,\ \cdots,\ 10$ according to Eqs. (4.16) and (4.21).
4. Compute P_0 according to Eq. (4.23).
5. Generate a random integer $m \in \{0,\ 1,\ \cdots,\ 10\}$ with probabilities $\{P_0,\ P_1,\ \cdots,\ P_{10}\}$. This is the number of secondary electrons emitted.[2]
6. If $m = 0$, the incident electron is absorbed without emission; proceed with the next electron.
7. If $m \neq 0$, generate m random polar angles $\theta_k \in (0, \pi/2)$ with probability distribution $\cos\theta$, and m random azimuthal angles $\phi_k \in (0, 2\pi)$ with uniform probability distribution. These angles determine the directions of the m emitted electrons relative to the normal at the surface.
8. Compute $P_{m,ts}$ from Eq. (4.21) and then F_m from Eq. (4.20).
9. If $m = 1$, generate a random kinetic energy $E \in (0, E_0)$ with probability density $f_{1,e} + f_{1,r} + f_{1,ts}$.
10. If $m \geq 2$, generate m random kinetic energies $E_k \in (0, E_0)$ with probability density $f_{m,ts}$. If the total energy $E_1 + \cdots + E_m$ exceeds E_0, regenerate all the E_k's. Repeat, if necessary, until the total energy does not exceed E_0. These are the chosen energies for the secondary electrons.

5 Beam-electron interaction.

5.1 The transverse electric field.

For simplicity, we assume that the bunch travels at the speed of light and has a charge density ρ that is factorized into a longitudinal part λ and a transverse part $\rho_\perp$ so that, at time t, it is given by

$$\rho(x, y, s, t) = \lambda(s - ct)\rho_\perp(x, y) \tag{5.1}$$

where s is the direction down the chamber, and x, y are the transverse coordinates. We choose $\rho_\perp$ to be normalized to unity so that it has dimensions of inverse area; this implies that λ has dimensions of charge per unit length:

$$\int dxdy\, \rho_\perp(x, y) = 1, \qquad \int ds\, \lambda(s) = \text{total bunch charge} = eN_p \tag{5.2}$$

[2] We have never seen more than 9 electrons being generated in a single collision.

It can then be shown from Maxwell's equations that the longitudinal part of the electric field $\mathbf{E}$ vanishes while the transverse part is proportional to λ,

$$E_z = 0, \tag{5.3a}$$

$$\mathbf{E}_\perp = (E_x, E_y) = \lambda(s - ct)\mathbf{F}(x, y) \tag{5.3b}$$

where $\mathbf{F}$ is a two-component vector that satisfies the two-dimensional Poisson equation,

$$\nabla \cdot \mathbf{F} = 4\pi\rho_\perp(x, y) \tag{5.4}$$

Since the field is effectively two-dimensional, it is extremely convenient to use complex notation to represent it [15]. Thus we define the "complex electric field,"

$$\mathcal{E} \equiv F_x + iF_y \tag{5.5}$$

It should be noted that $\mathbf{F}$ (and therefore $\mathcal{E}$) has dimensions of 1/length rather than charge/length^2 because we have explicitly factored out the linear charge density λ in Eq. (5.3). Thus $\mathcal{E}$ is the electric field per unit linear charge density and not the electric field itself.

For an infinitely-thin line of charge located at the point (x_0, y_0) inside an elliptical chamber of semi-axes (a, b), with $a > b$ and a along x, the solution of the transverse Poisson equation subject to perfect-conductor boundary conditions is most conveniently expressed in elliptic coordinates (μ, ϕ) [8],

$$\mathcal{E} = \frac{2}{\bar{z} - \bar{z}_0} + \frac{4}{g}\sum_{n=1}^{\infty} e^{-n\mu_1}\left[\frac{\cosh n\mu_0 \cos n\phi_0}{\cosh n\mu_1} + i\frac{\sinh n\mu_0 \sin n\phi_0}{\sinh n\mu_1}\right]\frac{\sinh n\bar{q}}{\sinh \bar{q}} \tag{5.6}$$

where the bar denotes complex conjugation; $z \equiv x + iy \equiv g\cosh q$ with $q \equiv \mu + i\phi$ being the elliptic coordinates in complex form of the observation point (x, y); $z_0 = x_0 + iy_0 = g\cosh(\mu_0 + i\phi_0)$; and where

$$g = \sqrt{a^2 - b^2}, \qquad \mu_1 = \frac{1}{2}\log\left(\frac{a + b}{a - b}\right) \tag{5.7}$$

The first term in Eq.(5.6) represents the field from the "direct" charge, and the series is the contribution from the surface charges.[3] It is straightforward to show that the series converges absolutely whenever (x, y) is inside the chamber.

Now the transverse distribution of the beam is approximately gaussian with rms sizes σ_x, σ_y which are much smaller than the transverse dimensions of the chamber. At distances beyond a few σ's from the beam, the details of the beam distribution are not important, while the surface charges become more and more important as the observation point approaches the walls of the chamber. Therefore in this region we approximate the field by that of a thin line of charge located at the bunch centerline using Eq. (5.6). Near the beam the field from the surface charges is negligible so we can approximate the field by the direct component, given by the Bassetti-Erskine formula [16]. To simplify the calculation even further, we use the linearized form of this formula inside the 1-σ ellipse. In summary, for the field calculation in our simulation we use

$$\mathcal{E} = \begin{cases} \dfrac{2(\xi - \xi_0)}{\sigma_x + \sigma_y} & \text{for } |\xi - \xi_0| \le 1 \\ \text{Eq. (5.6)} & \text{for } |\xi - \xi_0| > 1 \end{cases} \tag{5.8}$$

where the bunch center is assumed to be at location (x_0, y_0), and we have defined $\xi = x/\sigma_x + iy/\sigma_y$ and $\xi_0 = x_0/\sigma_x + iy_0/\sigma_y$. This "patched" field has the advantage of simplicity but it has the unphysical feature of being discontinuous at $|\xi - \xi_0| = 1$. In general we do not expect this feature to be very important because the ECI is dominated by electrons outside this region.

[3] It should be noted that the n-th term in the series does *not* represent an image charge.

5.2 Round-chamber limit.

It is interesting and useful to obtain the limit of expression (5.6) for a round chamber of radius a. This limit is defined by $g \to 0$ and $\mu, \mu_0, \mu_1 \to \infty$ such that $ge^{\mu+i\phi} = \text{fixed} = z$, $ge^{\mu_0+i\phi_0} = \text{fixed} = z_0$, and $ge^{\mu_1} = \text{fixed} = a$. In this limit, the series in Eq. (5.6) turns into a geometric series that can be immediately summed, yielding the well-known result

$$\mathcal{E} = \frac{2}{\bar{z} - \bar{z}_0} - \frac{2}{\bar{z} - \bar{z}_i} \tag{5.9}$$

where $\bar{z}_i \equiv a^2/z_0$. The second term has the immediate interpretation of representing a single image line charge whose density is equal and opposite to that of the beam, and which is located outside the chamber at the point conjugate to the beam, $z_i = a^2/\bar{z}_0$.

5.3 Impulse approximation.

Let $\mathbf{E}$ and $\mathbf{B}$ be the electric and magnetic fields produced by the bunch, and let $\mathbf{v}_-$ and $-e$ be the velocity and charge of an electron. Its equation of motion is, then,

$$\frac{d\mathbf{p}}{dt} = -e\left(\mathbf{E} + \frac{\mathbf{v}_-}{c} \times \mathbf{B}\right) \simeq -e\mathbf{E} \tag{5.10}$$

where we have neglected the magnetic force on account of the assumption that the electron is nonrelativistic (just like $\mathbf{E}$, the magnetic field $\mathbf{B}$ is also purely transverse, and its magnitude is comparable to that of $\mathbf{E}$). Thus the momentum change, in the impulse approximation, is obtained by integrating this equation over time assuming that the electron does not move during the bunch passage,

$$\Delta\mathbf{p} = \int_{-\infty}^{\infty} dt\, \frac{d\mathbf{p}}{dt} = -\frac{e^2 N_p}{c}\mathbf{F} \tag{5.11}$$

where we have used Eq. (5.2), and where $e^2/c \simeq 1.44 \times 10^{-9}$ (eV/c)–m. In terms of the complex electric field $\mathcal{E}$, Eq. (5.11) reads

$$\Delta p_x + i\Delta p_y = -\frac{e^2 N_p}{c}\,\mathcal{E} \tag{5.12}$$

5.4 Kick experienced by the photoelectrons.

As explained in Sec. 2.5, the space and time structure of the photoelectric process is important because, when the beam traverses a dipole bending magnet, the photons that are generated have the same time structure as the beam. In particular, if a bunch has a gaussian longitudinal charge density with rms length σ_z, so does the pulse of photons generated by this bunch. If the photon reflectivity is specular and if $R \sim 1$, the photon pulse travels approximately together with the positron bunch even after several bounces. Thus the photoelectrons are produced *concurrently with the bunch* as it traverses a given chamber section. Since the photoelectric process is probabilistic, a given photoelectron may experience the full kick from the bunch if it is generated at the head of the pulse, or a small fraction of the kick if it is generated at the tail. In general, for a longitudinal gaussian distribution with an rms length $\sigma_t = \sigma_z/c$, the beam kick experienced by a photoelectron upon being generated is given by Eq. (5.12) weighted by the factor

$$\int_{t_{cr}}^{\infty} dt\hat{\lambda}(t) = \frac{1}{2}\left(1 - \text{erf}\left(\frac{t_{cr}}{\sqrt{2}\sigma_t}\right)\right) \tag{5.13}$$

where t_{cr} is the creation time of the photoelectron relative to the instant of passage of the center of the bunch and $\hat{\lambda}(t)$ is the normalized longitudinal charge distribution of the bunch as a function of time t. Of course, these electrons will receive a full kick from successive bunches.

5.5 Estimate of the largest kick.

It is of interest to obtain an estimate of the largest kick an electron can receive from a bunch passage. The peak value of the electric field from a gaussian bunch is $|\mathcal{E}| \simeq 2/(\sigma_x + \sigma_y)$ and this value is obtained at the 1-σ ellipse. If an electron remained at this location through the bunch passage, it would experience the kick

$$\Delta p \simeq -\frac{e^2 N_p}{c} \frac{2}{\sigma_x + \sigma_y} \tag{5.14}$$

where we have used Eq. (5.8), and its energy change would be

$$\Delta E = \frac{(\Delta p)^2}{2m} \simeq \frac{1}{2} mc^2 \left(\frac{2N_p r_e}{\sigma_x + \sigma_y} \right)^2 \tag{5.15}$$

where $r_e = e^2/mc^2 \simeq 2.818 \times 10^{-15}$ m is the classical radius of the electron. For PEP-II parameters, listed in Table 2, we obtain $\Delta E \simeq 18$ keV. If bunch-length effects are taken into consideration by slicing the bunch, the largest kick kick is only ~ 10 keV due to the electron movement during the bunch passage.

5.6 Estimate of the kicks received by electrons near the wall.

It is also instructive to have an idea of the magnitude of the smallest kick received by an electron. If an electron is close to the wall of the chamber, we can safely assume that the bunch is effectively point-like, and we can then estimate the field from Eq. (5.6).

We look only at the at the "corners"of the ellipse, *i.e.*, $(x, y) = (a, 0)$, with elliptic coordinates $(\mu, \phi) = (\mu_1, 0)$, and $(x, y) = (0, b)$, where $(\mu, \phi) = (\mu_1, \pi/2)$. If the beam is located at the center of the ellipse, only $n =$ even terms contribute in Eq. (5.6), and the convergence of the series is roughly controlled by the parameter

$$e^{-2\mu_1} = \frac{a-b}{a+b} \tag{5.16}$$

which has the value $e^{-2\mu_1} \simeq 0.29$. Thus, to first approximation, we obtain

$$\mathcal{E}_y(x = 0, y = b) \simeq \frac{2}{b} + \frac{8e^{-2\mu_1}}{g} \frac{\sinh \mu_1}{\cosh 2\mu_1} \tag{5.17a}$$

$$\mathcal{E}_x(x = a, y = 0) \simeq \frac{2}{a} - \frac{8e^{-2\mu_1}}{g} \frac{\cosh \mu_1}{\cosh 2\mu_1} \tag{5.17b}$$

Here the first term ($2/a$ or $2/b$) is the direct field, and the second is the contribution from the surface charges (notice the sign difference in the two). The corresponding numerical values are

$$\mathcal{E}_y(x = 0, y = b) \simeq 0.80 + 0.22 = 1.02 \quad \text{cm}^{-1} \tag{5.18a}$$

$$\mathcal{E}_x(x = a, y = 0) \simeq 0.44 - 0.39 = 0.05 \quad \text{cm}^{-1} \tag{5.18b}$$

In the impulse approximation, the corresponding energy kick received by an electron at rest is $\Delta E = (mc^2/2)(r_e N_p |\mathcal{E}|)^2$, which yields

$$\Delta E(x = 0, y = b) \simeq 67 \quad \text{eV} \tag{5.19a}$$

$$\Delta E(x = a, y = 0) \simeq 0.2 \quad \text{eV} \tag{5.19b}$$

and the corresponding velocity kicks are

$$\Delta v_y(x = 0, y = b) \simeq 0.5 \quad \text{cm/ns} \tag{5.20a}$$

$$\Delta v_x(x = a, y = 0) \simeq 0.02 \quad \text{cm/ns} \tag{5.20b}$$

Eq. (5.19b) shows that the kick from the beam at the horizontal corners of the chamber, $x = \pm a,\ y = 0$, is smaller than the typical energy (~ 5 eV) with which a photoelectron is created. Eq. (5.20a) shows that an electron created at $x = 0,\ y = \pm b$ will travel, in a field-free region, ~ 2 cm during one bunch spacing of ~ 4 ns. Therefore the natural time scale for the electrons to cross the vacuum chamber is $\sim 8 - 12$ ns, which corresponds to a few bunch passages. If the electron in question is a "just-born" photoelectron, the estimate for the kick is further reduced by the factor given by Eq. (5.13), with a concomitant increase in the traversal time.

5.7 Criterion for the validity of the impulse approximation.

The impulse approximation used in Eq. (5.11) is valid provided that the forces act on a time scale so short that the electron remains essentially at rest during this time. A practical criterion for the validity of this approximation in the absence of a magnetic field can be found as follows: Consider an electron at rest (or moving sufficiently slowly) at a distance r from the beam, where $r \gg \sigma_x, \sigma_y$. Neglecting surface charges, the momentum kick is given by Eq. (5.11), namely

$$\Delta p \simeq -\frac{e^2 N_p}{c}\,\frac{2}{r} \tag{5.21}$$

For a weak enough kick the electron remains nonrelativistic, and the corresponding velocity change is $\Delta v = \Delta p/m$. The characteristic length of time during which the field acts on the electron is σ_t, the rms bunch length in units of time. During this time the electron moves a distance $\Delta r = \Delta v \sigma_t$. Then the criterion for the validity of the impulse approximation is $\Delta r \ll r$, or $2e^2 N_p \sigma_t / mcr \ll r$. In terms of σ_z, the criterion is written

$$2N_p \frac{r_e \sigma_z}{r^2} \ll 1 \tag{5.22}$$

This criterion can be turned around to define a radius r_i that roughly determines the transverse region of validity of the impulse approximation. For this we choose 0.1 to be a practical measure of smallness in Eq. (5.22) so that

$$r_i = \sqrt{20 N_p r_e \sigma_z} \tag{5.23}$$

The impulse approximation is approximately valid for electrons that are at distances from the bunch larger than r_i at the time the bunch passes. For nominal PEP-II parameters, we obtain $r_i = 6$ mm which is small compared to the radius of the chamber. Therefore, the impulse approximation is valid for all electrons except those that are very close to the beam.

5.8 Bunch-length effects.

The standard way to improve upon the impulse approximation consists in dividing the bunch into several slices, which turn the bunch-electron interaction into a "thick-lens" kick [17]. Our code POSINST does allow for this slicing. As implied by Sec. 5.7, however, one expects these effects to be small for the case of PEP-II. Indeed, we have verified that this is the case in field-free regions, so that for these one can safely use the impulse kick defined by Eq. (5.12).

It turns out, however, that Eq. (5.12) is a poor approximation in the presence of a strong dipole magnetic field. In this case, for PEP-II nominal parameters, the electrons in the cloud are confined to move in tight vertical helices whose typical radius is a few microns and whose period is comparable to the bunch length σ_t. As a result, the horizontal beam-electron kick is phase-averaged over the cyclotron motion; this implies that bunch-length effects are expected to be important, as we have verified. The main consequence of this cyclotron-phase averaging is that the impulse approximation is still roughly valid provided it is modified according to [5]

$$\Delta p_x + i\Delta p_y = -\frac{e^2 N_p}{c}(S\mathcal{E}_x + i\mathcal{E}_y) \tag{5.24}$$

where we have assumed that the B field is along the y direction and where S is a cyclotron phase suppression factor given by

$$S = \int_{-\infty}^{\infty} dz\, \hat{\lambda}(z)\, e^{-i\omega z/c} \tag{5.25}$$

Here $\hat{\lambda}(z)$ is the longitudinal charge distribution of the bunch, normalized to unity, and $\omega = eB/mc$ is the cyclotron frequency of the electron in the field. For a gaussian bunch distribution, with $\hat{\lambda}(z) = e^{-(z/\sigma_z)^2/2}/\sqrt{2\pi}\sigma_z$, this yields

$$S = \exp\left(-\tfrac{1}{2}(\omega\sigma_t)^2\right) \tag{5.26}$$

For the case of PEP-II, with $\sigma_z = 1$ cm and $B = 0.752$ T, the cyclotron frequency of a nonrelativistic electron in a dipole bending magnet is $\nu = \omega/2\pi = 21$ GHz and therefore $S = 5.9 \times 10^{-5}$ which implies that the horizontal kick is strongly suppressed.

6 Space-charge forces.

Making the approximation that the density of the cloud is longitudinally uniform, we compute the space-charge forces from the electrons upon themselves by using a two-dimensional square grid and adding up the electric field (5.6) from all the electrons at all grid points. We then compute the fields at the actual location of the electrons by using an area-weighted interpolation [18]. Typically we use a 5×5 mm grid cell, with spot checks using 1×1 mm. We compute the space-charge field once following a bunch passage, but we apply it on the electrons a certain number of times in between successive bunches, typically 4, with spot checks to 8. However, as explained below, the space-charge forces are quite weak as a result of the low equilibrium density of the electron cloud, so it is a good approximation to neglect them in most applications to PEP-II.

7 Calculation of the wake function and ECI growth rate.

For the calculation of the wake function we follow the conventions of Ref. [19]. Let Δp_y be the momentum kick experienced by the "trailing bunch" as it traverses a single section of length L keeping a fixed distance z behind the "perturbing bunch" while being displaced by Δy from the central orbit. Assuming that there are N such sections in the ring, their aggregate contribution to the dipole wake is given by

$$W_y(z) = -\frac{NL\bar{F}_y}{qQ\Delta y} = -\frac{cN}{(eN_p)^2} \cdot \frac{\Delta p_y}{\Delta y} \tag{7.1}$$

where $\bar{F}_y$ is the average force experienced by the trailing bunch as it traverses one section, namely $\bar{F}_y = \Delta p_y/\Delta t$ with $\Delta t = L/c$. Now, in the simulation, we compute Δp_y from the macroparticles that represent the electrons in the cloud. Therefore, the actual value for the wake function is obtained by replacing

$$\frac{\Delta p_y}{\Delta y} \to \frac{\Delta p_y}{\Delta y} \times \mathcal{F} \tag{7.2}$$

where $\mathcal{F}$ is the macroparticle-to-particle charge ratio, discussed below.

From the dipole wake function we compute the coherent multibunch oscillation frequency from standard first-order formulas [19]. For the case of M equally-spaced, equally-charged bunches, the coherent dipole frequency Ω_μ of oscillation mode μ is given, in first-order perturbation theory [19], by

$$\Omega_\mu - \omega_\beta = \frac{ce^2 N_p}{4\pi E\nu_\beta} \sum_{k=0}^{M-1} W(ks_B) e^{2\pi i k(\mu+\nu_\beta)/M} \tag{7.3}$$

where $\omega_\beta = \omega_0\nu_\beta$ is the betatron angular frequency, ν_β is the tune of the ring, $\mu = 0, 1, \cdots, M-1$ is the collective mode oscillation number, and E is the beam energy. This formula assumes that the range

of the wake is short compared to the betatron wavelength; this assumption is well satisfied in all cases we consider here. In the above formula the bunch centroid is assumed to oscillate according to $y^{(\mu)}(t) \propto \exp(-i\Omega_\mu t)$. Therefore, by writing $\Omega_\mu = \mathrm{Re}\,\Omega_\mu + i\,\mathrm{Im}\,\Omega_\mu$, one sees that the mode is unstable (amplitude grows exponentially in time) when $\mathrm{Im}\,\Omega_\mu > 0$, and damped when $\mathrm{Im}\,\Omega_\mu < 0$. Also, in Eq. (7.3), W represents either the horizontal or the vertical dipole wake function, and ν_β is the corresponding tune. Thus the resultant coherent frequencies $\Omega_{\mu,x}$ and $\Omega_{\mu,y}$ are, in general, different from each other.

The $k = 0$ term in Eq. (7.3) leads to a purely real contribution to Ω_μ that is independent of the mode number μ. Therefore this term has the interpretation of being an overall coherent tune shift, and is given by

$$\Delta\nu_\beta = \frac{e^2 C N_p}{8\pi^2 E \nu_\beta} W(0) \tag{7.4}$$

where C is the circumference of the ring.

Our simulation results show that the wake function is positive and short-ranged, *i.e.*, $W(s_B) \gg |W(ks_B)|$ for all $k \geq 2$. As a result, one immediately obtains from Eq. (7.3) an estimate for the instability growth rate from the $k = 1$ term, which we call τ_0^{-1},

$$\tau_0^{-1} \simeq \frac{ce^2 N_p}{4\pi E \nu_\beta} |W(s_B)| \tag{7.5}$$

where we have used the fact that, for $M \gg 1$, the mode $\mu \simeq M/4$ is such that the phase factor in Eq. (7.3) is very close to i. This is the most unstable mode, and it is this mode whose growth rate is given by Eq. (7.5).[4]

If the beam is not equally populated but has a gap, as is usually the case, the unstable modes do not grow exponentially in time if the range of the wake function is short compared with the length of the bunch train. In this situation the amplitude growth follows a power law rather than an exponential [19]. For example, in the simplest case, in which the wake function vanishes at distances beyond one bunch spacing, the amplitude of the n-th bunch grows like $y_n(t) \propto (t/\tau_0)^{n-1}$ where we take the convention that the head bunch is labeled $n = 1$. The important thing is that, in this formula, τ_0 is *the same quantity* given by Eq. (7.5). Since the amplitude of the trailing bunches in the train grows with a large power when $M \gg 1$, there is no practical difference between the beam-gap case and the uniformly-populated-beam case.

8 Simulation procedure.

Our program "POSINST" simulates the dynamics of the electron cloud and computes the effective wake function following the same ideas as in ref. [3]. The code simulates the cloud within a single specified section of the ring and evaluates, in addition to the wake function, various statistical quantities and spectra of the electron cloud. Basic PEP-II parameters used in our simulations are shown in Tables 1 and 2.

A basic input to the simulation is the time-averaged number of photoelectrons per bunch passage, $\bar{N}_e$, given by Eqs. (2.14) or (2.17). These photoelectrons are represented by a *fixed number* of macroparticles, N_{phel}. These are generated at every bunch passage at the walls of the section being simulated. If $R \sim 1$, they are distributed uniformly (both transversely and longitudinally) around the chamber, with a gaussian distribution in kinetic energy that peaks at 5 eV and has a width of 5 eV. If $R \sim 0$, the photoelectrons are generated just above and just below the antechamber slot, and their total numbers in a pumping section and in a dipole bending magnet are given by Eq. (2.17). The angles of the photoelectrons are generated with a $\cos\theta$-distribution where θ is the angle relative to the normal to the surface at the point of emission. These electrons are then kicked by the successive bunches that traverse the section. When the electrons collide at the chamber wall, they are either absorbed or create secondary electrons according to the secondary emission model described in Sec. 4. If they "hit" the wall at the location of the antechamber slot, they are removed from the simulation. The space-charge force is optionally included in the motion of the electrons in the cloud.

[4] If $W(s_B)$ is negative and such that $|W(s_B)| \gg |W(ks_B)|$ for all $k \geq 2$, the estimate for the growth rate is still given by Eq. (7.5). In this case, however, the most unstable mode, to which this growth rate corresponds, is $\mu \simeq 3M/4$.

Table 2: Parameters used in the ECI studies.

Ring circumference, C [m]	2199.32
No. of particles per bunch, N_p	5.63×10^{10}
Bunch spacing, s_B [m]	1.26
No. of bunches (no gap), M	1746
Tunes, (ν_x, ν_y)	$(38.57, 36.64)$
Vacuum chamber semi-axes, (a, b) [cm]	$(4.5, 2.5)$
Antechamber slot full height, h [cm]	1.5
Average rms bunch sizes, (σ_x, σ_y) [mm]	$(1, 0.2)$
RMS bunch length, σ_z [cm]	1
Pumping section length, L_{PS} [m]	7.15

We start the simulation by injecting a train of bunches into an empty vacuum chamber. We compute the dipole wake function by letting one bunch, say bunch number n, be displaced vertically from the equilibrium orbit by an amount Δy; this displaced bunch perturbs the electron cloud. We then measure the momentum kick Δp_y arising from this perturbation on bunches $n+1$, $n+2$, etc, which are themselves not displaced, and obtain the wake function from Eq. (7.1) for $z = 0$, s_B, $2s_B$, etc.

In practice, one cannot simulate the electron cloud with a realistic number of particles, which is expected to be in the range $10^8 - 10^{10}$ per section, since this number is too large for present-day computers. Thus one resorts to simulating a much smaller number of representative particles, usually referred to as "macroparticles." In order to obtain quantitative results from the simulation which can be compared with a real machine, one must scale all electron-density-dependent quantities obtained from the simulation by a density factor $\mathcal{F}$, which can also be interpreted as the macroparticle-to-particle charge ratio, given by

$$\mathcal{F} = \frac{\text{number of electrons in reality}}{\text{number of electrons in the simulation}} \tag{8.1}$$

Neither the numerator nor the denominator in Eq. (8.1) is known a priori, so we need a more convenient expression to compute the density factor $\mathcal{F}$. Since the basic input value to our simulation is the number of macro-photoelectrons per bunch passage, N_{phel}, we can express $\mathcal{F}$ as

$$\mathcal{F} = \frac{\bar{N}_e}{N_{\text{phel}}} \tag{8.2}$$

The numerator in this formula is the total number of real photoelectrons created in the section being simulated during a time interval equal to a bunch spacing, s_B/c, while the denominator is the corresponding number of macro-photoelectrons. Eqs. (8.2) and (8.1) are equivalent because the number of electrons in existence in the simulation (and in reality) is directly proportional to the number of photoelectrons.

9 Results.

In this article we use a slightly better fit to the SEY data than we used in our previously published results [5]. Our present results for the growth rates are not qualitatively different, but we have analyzed the electron cloud itself and the wake functions in more detail.

9.1 Energy distribution of electrons hitting the wall.

A consequence of the kick modulation discussed in Sec. 2.5 is an approximately uniform momentum distribution of the photoelectrons immediately following the passage of the bunch that created them. To see this

we note that the time distribution of the generated photoelectrons is

$$\frac{dN}{dt} \propto \int_{t_{cr}}^{\infty} dt \hat{\lambda}_\gamma(t) \tag{9.1}$$

where $\hat{\lambda}_\gamma(t)$ is the time distribution of the photon pulse and $t = 0$ is the instant of passage of the center of such a pulse. Following the passage of the bunch, the photoelectrons have a momentum

$$p = \Delta p + p_0 \tag{9.2}$$

where Δp is the kick from the beam and p_0 is the intrinsic momentum from the photoelectric process. Now using Eq. (5.13) we obtain

$$\frac{dN}{dp} = \frac{dN}{dt_{cr}} \frac{dt_{cr}}{dp} \propto \frac{\hat{\lambda}_\gamma(t)}{\hat{\lambda}(t)} = 1 \tag{9.3}$$

where we have have neglected dp_0/dt_{cr} and have set $\hat{\lambda}_\gamma(t) = \hat{\lambda}(t)$, as discussed in Sec. 5.4. This uniformity of the momentum distribution has the effect of smoothing out the initial clumpiness of the photoelectron distribution. The modulation of the photoelectron kick, Eq. (5.13), leads to a low-energy tail in the distribution of electrons hitting the wall, as seen in Fig. 10.

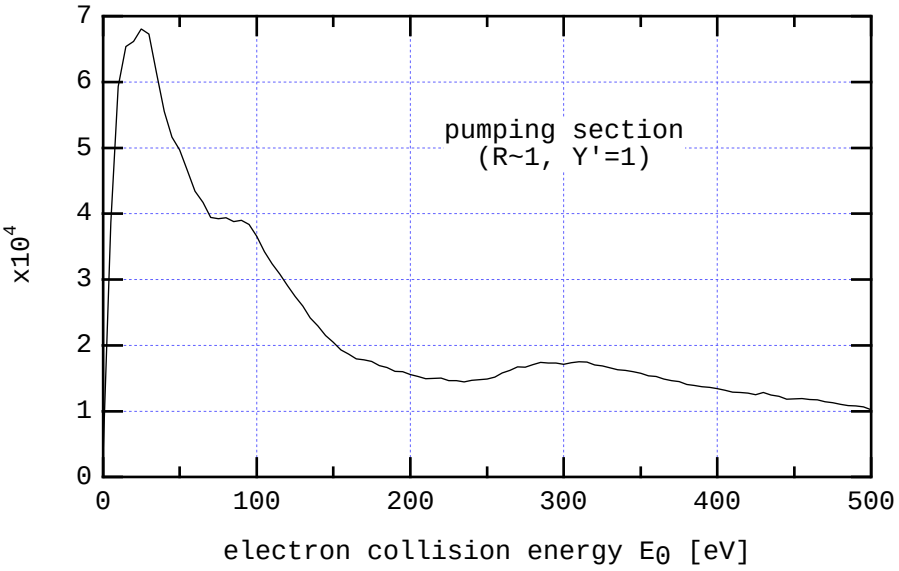

Figure 10: The unnormalized kinetic energy spectrum of the electrons hitting the walls of the vacuum chamber in a pumping section, obtained for $Y' = 1$ and $R \sim 1$. The spectrum extends out to $E_0 \sim 20$ keV in agreement with the estimate in Sec. 5.5.

9.2 Pumping sections.

Under nominal PEP-II operating conditions, and assuming a photon reflectivity $R \sim 1$ and a photoelectric efficiency $Y' = 1$, the number of photoelectrons generated at the vacuum chamber walls of a given pumping section during a time interval s_B/c, given by Eq. (2.14), is $\bar{N}_e = 6.3 \times 10^8$ (this value includes a dilution factor $\mathcal{D} = 0.66$, Eq. (2.15)). Figure 11 shows the development of the electron cloud in a pumping section. One can see that an equilibrium is reached after ~ 25 bunch passages, at which point the average electron

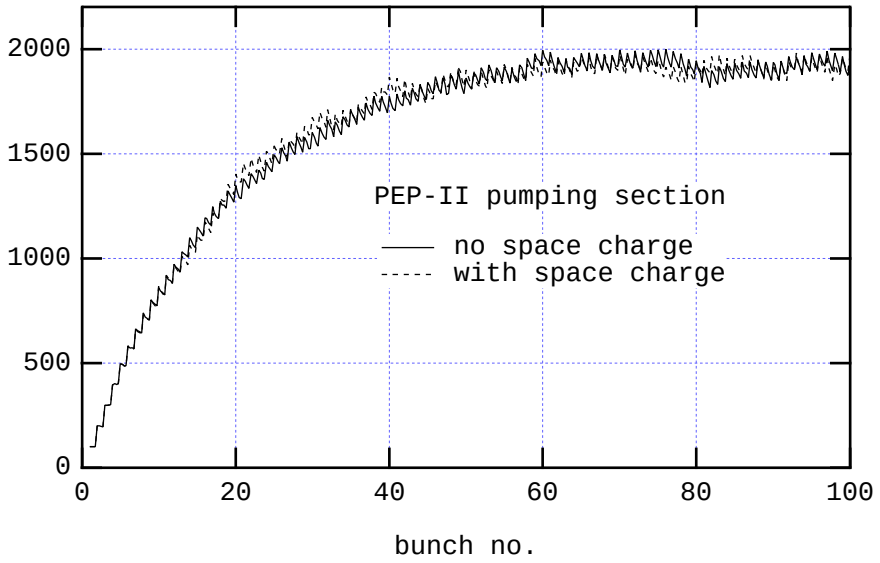

Figure 11: The build-up of the electron cloud as a function of time, measured in bunch passages. The lines represent the total number of macroparticles contained in a given pumping section. The simulation was done for $Y' = 1$, $R \sim 1$ and $\hat{\delta}_t = 1.066$, and was obtained by launching $N_{\rm phel} = 100$ new macro-photoelectrons per bunch passage, with and without the space-charge forces. These forces were obtained from a 5×5 mm grid, and the bunch spacing was divided into 4 steps. This case with low statistics has a relatively high ratio of macroparticle-to-particle charge, $\mathcal{F} = \bar{N}_e/N_{\rm phel} = 6.27 \times 10^6$.

density stabilizes at $\sim 3.2\%$ of the neutralization level (the neutralization density d_n is the average electron density such that the beam charge is neutralized, *i.e.*, $d_n = N_p/\pi abs_B = 1.27 \times 10^7$ electrons/cm^3).

The electron cloud reaches an equilibrium because the "effective SEY," *i.e.*, the SEY averaged over all the electron-wall collisions, is, in this case, ~ 0.85. Since this number is < 1, the vacuum chamber walls act as a net absorber of electrons, and therefore an equilibrium is reached when the number of electrons absorbed by the wall during one bunch passage equals the number of new photoelectrons generated during such a time. It should be emphasized, however, that the density distribution is time-dependent; furthermore, its time-average is not spatially uniform, as seen in Fig. 12.

Due to the relatively low density the space-charge forces are weak, as evidenced by the closeness of the two curves in Fig. 11. For this reason we neglect these forces in all other simulations presented here. The same is true for the dipole bending magnets. This approximation results in a considerable savings of computer time. It would not be valid for uncoated aluminum chambers, where the peak value of the SEY is ~ 2. In that case, the effective SEY is > 1, and the electron cloud density increases exponentially in time until it reaches the neutralization level, at which point it stops growing as a consequence of the space-charge forces. Obviously, in that case, one cannot neglect these forces in the simulation.

For the purposes of calculating the vertical dipole wake function we ran a simulation with higher statistics, namely $N_{\rm phel} = 10000$, and we displaced bunch no. 90 vertically by $\Delta y = 5$ mm in order to generate a wake. The result is shown in Fig. 13. One can see that the wake function decays very quickly following the perturbing bunch. The "short-range wake," *i.e.*, the value of the wake function at bunch no. 91, has the value $W_y(s_B) = 4.9 \times 10^4$ m^{-2}. From Eq. (7.5) we obtain the contribution to the growth rate from the pumping sections, $\tau_{0,PS}^{-1} = 840$ s^{-1}, and the coherent tune shift from Eq. (7.4), $\Delta\nu_{\beta y} = 0.0024$. By applying Eq. (7.3) to the wake function in Fig. 13 for $k = 1, \cdots, 10$ we obtain the coherent mode spectrum, shown in Fig. 14. The approximately sinusoidal shape of the curve is a direct consequence of the fact that the value of the wake function at $z = s_B$ dominates over all others. As discussed earlier, the most unstable mode is

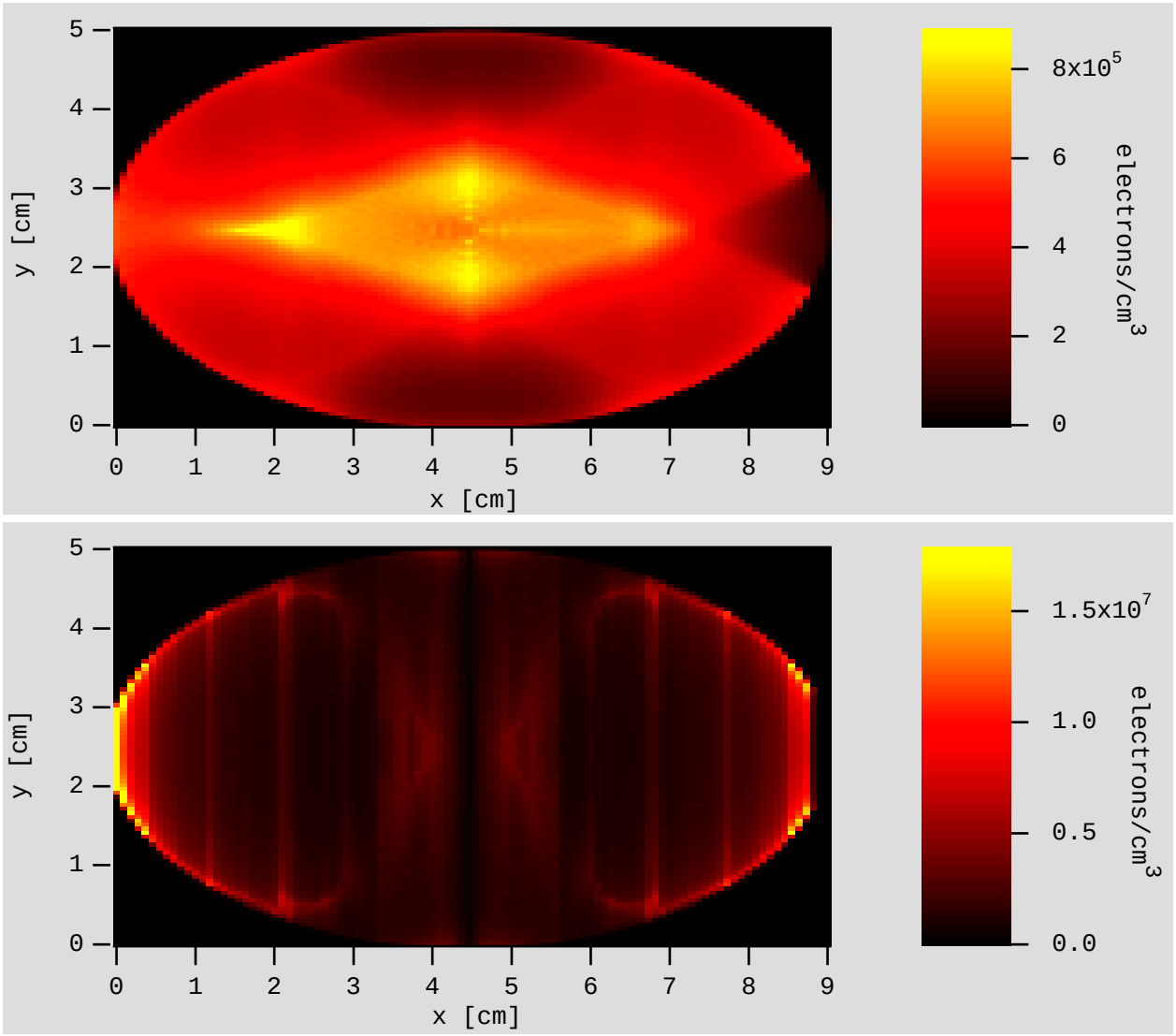

Figure 12: Image of the time-averaged density of the electron cloud in a pumping section (top) and in a dipole bending magnet (bottom) for $Y' = 1$, $R \sim 1$ and $\hat{\delta}_t = 1.066$. The low-density area to the right of the top plot is due to the electrons escaping to the antechamber slot. In the bottom image one can see vertical regions of high density where electrons tend to concentrate (the bright areas at the horizontal edges, however, are an artifact of the plot.

$\mu \simeq M/4$, and from the corresponding peak value of the spectrum we also obtain the estimate $\tau_{PS}^{-1} = 840$ s^{-1} for the growth rate. The reason for this equality is that, as it can be seen in Fig. 13, the wake is almost exactly out of phase with the bunches after bunch no. 91. This feature is probably an accident arising from the detailed choices of parameter values.

For the case $R \sim 0$ a similar calculation yields $\tau_{0,PS}^{-1} = 1240$ s^{-1} and $\tau_{PS}^{-1} = 1300$ s^{-1}. The average electron density stabilizes at $\sim 5.6\%$ of the neutralization level, the effective SEY is 0.86, and the vertical coherent tune shift is 0.0040.

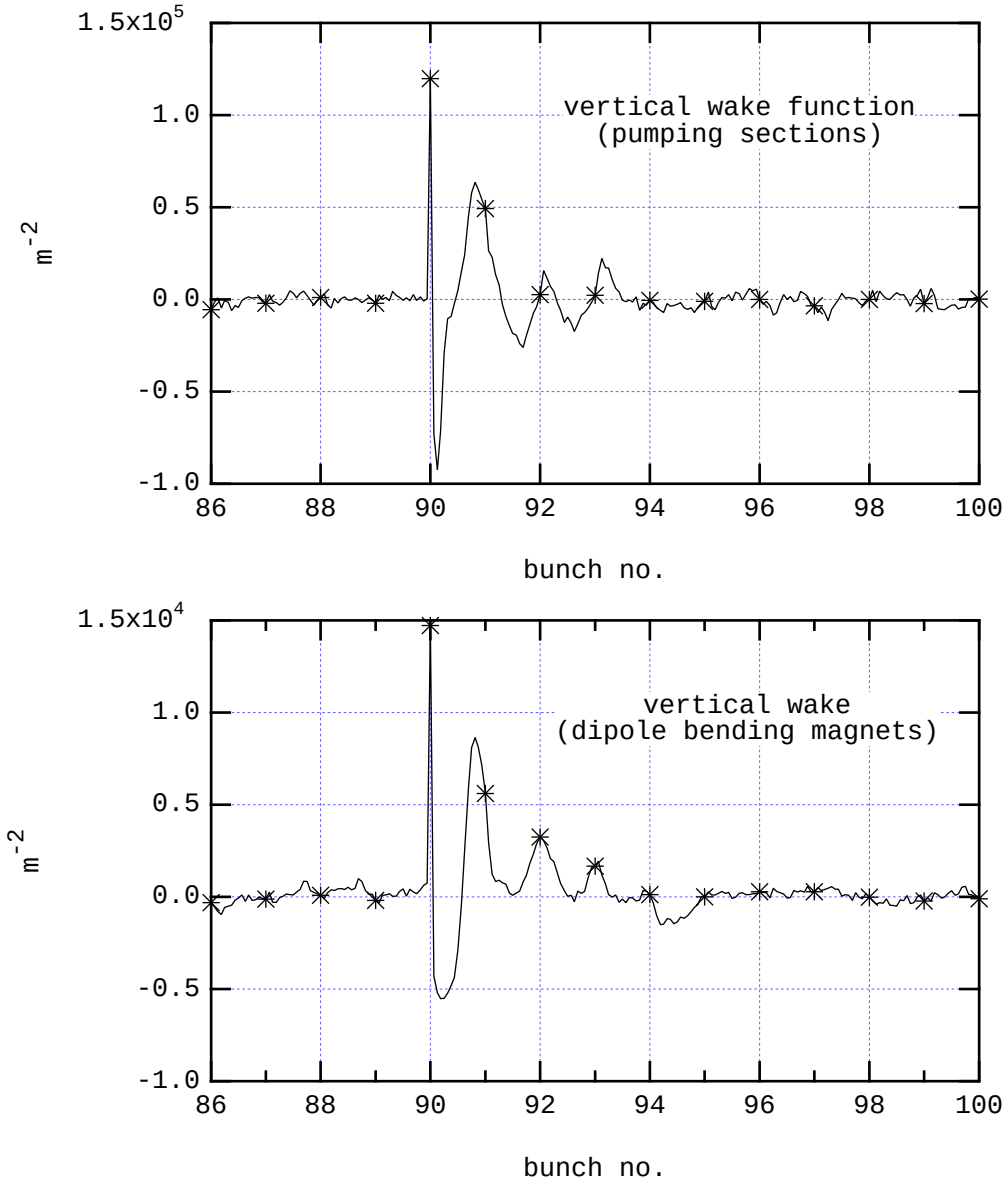

Figure 13: The vertical dipole wake function for the PEP-II pumping sections and the dipole bending magnets for $Y' = 1$, $R \sim 1$ and $\hat{\delta}_t = 1.066$. The simulation was obtained by launching $N_{\rm phel} = 10000$ new macro-photoelectrons per bunch passage. Bunch number 90 was then displaced vertically by 5 mm in order to generate a wake. Ideally, the wake should vanish identically for bunches 1–89; the fact that it does not is a reflection of the statistical noise of the computation. Asterisks are located at integer intervals, emphasizing the actual bunch locations. It is only these locations that contribute to the growth rate. Note that the vertical scales are different by an order of magnitude.

9.3 Dipole bending magnets.

If we assume $R \sim 1$, the electron cloud saturates at an average density $\sim 1.1 \times 10^6$ electrons/cm^3, which corresponds to $\sim 9.1\%$ of the beam neutralization level. The effective SEY is 0.45 and the coherent tune

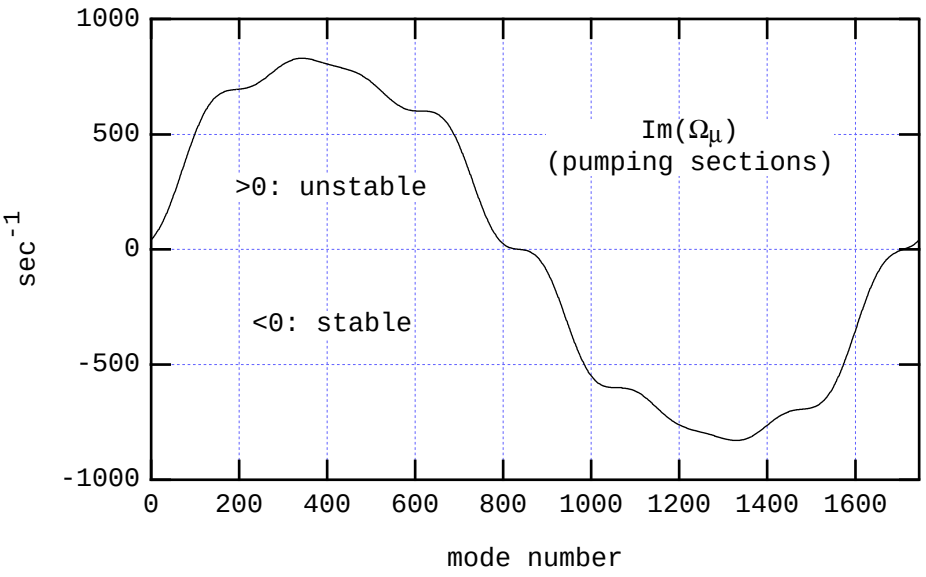

Figure 14: The imaginary part of the coherent mode spectrum, obtained by applying Eq. (7.3) to the pumping section wake function in Fig. 13 to bunches 91–100.

shift is 0.0003. Figure 12 shows the image of the time-averaged electron density.

The contribution to the growth rate of the ECI from all the dipole magnets in the ring, considering only the value of the wake function at $z = s_B$, is $\tau_{0,B}^{-1} = 96\ \mathrm{s}^{-1}$. In this case the wake function, shown in Fig. 13, is almost exactly in phase with the bunches. As a result, the growth rate computed from the coherent mode spectrum, Eq. (7.3), is $\tau_B^{-1} = 134\ \mathrm{s}^{-1}$, which is larger than $\tau_{0,B}^{-1}$ by 40%. The phase equality of the wake function and the bunches is probably an accident arising from the detailed parameter values in the model.

If we assume $R \sim 0$, the photoelectrons are generated only along narrow strips just above and just below the antechamber slot upon the photons' first strike. The trapping effect of the magnetic field causes the electrons to remain confined to a narrow vertical region in the neighborhood of the antechamber slot, which is far away (~ 4.5 cm) from the beam. In this case, the ionization of the residual gas by the beam contributes most of the electrons that are near the beam orbit. However, our simulations show that, even assuming a vacuum pressure 150 times larger than the nominally-specified 1 nTorr, the contribution to the ECI growth rate from the dipoles is only $\sim 1.5\ \mathrm{s}^{-1}$.

10 Conclusions.

10.1 Electron density and ECI growth rates.

We conclude that the contribution to the growth rate of the ECI from the combined effects of the pumping sections and the dipole bending magnets in the arcs of the PEP-II positron ring is $\tau^{-1} \sim 1000\ \mathrm{s}^{-1}$, and it is dominated by the pumping sections. This result assumes TiN-coated chambers with a peak SEY $\hat{\delta}_t = 1.066$, a photoelectric yield $Y' = 1$, and a photon reflectivity $R \sim 1$. If $R \sim 0$, the growth rate estimate is $\tau^{-1} \sim 1300\ \mathrm{s}^{-1}$ at $Y' = 1$. Such growth rates are within the range controllable by the feedback system [7].

In the near future we shall incorporate into our model for the SEY the actual measured incident-angle dependence. We do not expect that our results will change appreciably from those presented here. We have yet to evaluate the contribution to the ECI growth rate from other magnets and other regions of the ring, and to assess the effects of a temporary increase of the SEY from possible air exposure of the chamber. We expect that the interaction region "straight" section will contribute substantially to the growth rate owing

to its bending magnets and lack of antechamber. Furthermore, our analysis thus far applies to the coherent dipole multibunch mode in linear, *i.e.*, small amplitude, approximation, and the growth rates have been obtained by computing the dipole wake function assuming that the bunches are rigid charges. Therefore our approach does not shed any light on the ECI at saturation amplitudes, nor on higher-order coherent modes, nor on the possibility of emittance growth. Such effects remain to be investigated by more complete simulation techniques.

Our simulations carried out for other machines, such as the LHC [20] and KEKB, show that the electron-cloud effect can manifest itself in different ways in different machines owing to its dependence on many parameters. It seems unlikely, at this stage of our understanding, that one will be able to find simple rules to scale the results from one machine to another, so that each machine has to be studied separately.

10.2 Dependence of the ECI growth rate on Y'.

For $R \sim 1$ the electron cloud reaches equilibrium at an average density $\sim 3\%$ of the neutralization level in the pumping sections, and $\sim 9\%$ in the dipole bending magnets. The pumping sections dominate the ECI growth rate by a factor ∼7:1 over the bending magnets, mainly due to the weighting from their overall length. By removing this length factor we obtain $\tau_{PS}^{-1}/L \sim 0.6$ s^{-1}/m for the pumping sections and $\tau_B^{-1}/L \sim 1.6$ s^{-1}/m for the bending magnets. These numbers are in a ratio 0.4:1, which is in qualitative agreement with the ratio of the corresponding average equilibrium densities of the cloud. This implies that the growth rates scale roughly linearly with the average electron density independent of the magnetic field, at least in the parameter regime relevant to PEP-II. However, there are important differences in the details of the density distribution that may have significant dynamical effects on the growth rates, depending upon details of parameter choices.

As a result of the low average density, the space-charge forces are expected to have a negligible effect. We have verified that this is the case by running a few spot-checks with and without space-charge forces turned on. In the approximation that these forces are completely ignored, it is easy to prove that the growth rates scale exactly linearly with Y'. Although we do not yet have a measured value for Y' for our samples, recent measurements at CERN [21] for a copper surface under photon illumination with a roughly similar spectrum and incident angle as appropriate for PEP-II yields a value $Y' = 0.2$. If this is any indication for our case, the ECI growth rate estimates will be 20% of those presented here.

10.3 Benefits of the antechamber and TiN coating.

The low values of the equilibrium electron densities mentioned above are a direct consequence of the fact the SEY of TiN is sufficiently low. Our simulations also show that, if the chambers were not coated with TiN, the electron cloud would be in a runaway condition by virtue of which the electron cloud density grows exponentially in time until it reaches an average value comparable to the beam neutralization level after ~ 100 bunch passages. At this point the growth stops due to the strong space-charge forces. By scaling our results with the average electron density at equilibrium, we estimate the growth rate of the ECI in the absence of the coating would be $\sim 20 - 30$ times larger than with the coating (this is probably a worst-case estimate; we have not carried out a reliable simulation of this situation). In this case the ECI growth rate would be fairly insensitive to the detailed values of R, Y' and the precise value of the peak SEY $\hat{\delta}_t$ as long as this latter is above some critical value. The values of these parameters would determine only how *quickly* the electron cloud reaches saturation, but not the level of the density itself, which would then be controlled only by the space-charge forces.

The measured peak value of the SEY, $\hat{\delta}_t = 1.066$, was obtained after a dose of 10^{18} electrons/cm^2 at an energy of 1100 eV. We expect that, when the beam is first injected into the machine, $\hat{\delta}_t$ will be higher than 1.066. Our simulations show that the average bombardment electron energy in the pumping sections is 870 eV, and the bombardment rate is 3.2×10^4 electrons/cm^2/ns. At this rate, we estimate that a dose of 10^{18} electrons/cm^2 will be achieved after ~ 18 A-h of integrated beam charge, which should be reached within the first few weeks of commissioning (the bombardment rate in the dipole bending magnets is higher, 6.5×10^4

electrons/cm^2/ns, but the average bombardment energy is lower, $\sim$ 200 eV; perhaps these two trends cancel each other out in their effect of reducing $\hat{\delta}_t$).

As mentioned in Sec. 2.1, the antechamber slot allows $\sim$ 99% of the radiated photons to escape from the vacuum chamber. Thus, in the absence of an antechamber, there would be 2 orders of magnitude more photons in the vacuum chamber. This does not imply a proportionally larger number of photoelectrons because the photons would have a higher average energy, for which the quantum efficiency is lower. A reasonable guess is that there would be 10 times more photoelectrons, implying that the ECI growth rate would be 10 times larger than without the antechamber. However, if the chamber were not coated with TiN, the benefit of the antechamber would be negligible *vis à vis* the ECI because the electron cloud density would reach the neutralization level anyway.

10.4 Bunch-length effects.

As mentioned in Sec. 5.8, our simulation code allows for slicing the bunch into a specified number of kicks in order to account for bunch-length effects. We have verified that, for the pumping sections, the bunch length has a negligible effect on the growth rate, although it does cut the high energy tail of the electrons hitting the chamber walls from the $\sim$ 20 keV impulse-approximation estimate down to $\sim$ 10 keV. Bunch-length effects are more important for the dipole bending magnets. In this case, however, we have substituted for the bunch slicing, which can amount to a considerable computational expense, a simple but accurate analytical modification of the impulse approximation.

10.5 Horizontal wakes.

We have carried out a few calculations of the horizontal wake function, but have not studied this case in detail. Results show that the horizontal growth rates are quite comparable with the vertical. We shall investigate this issue further in the future.

11 Acknowledgments.

We are indebted to R. Kirby and F. King for providing data on SEY before publication. For useful discussions we wish to thank J. Bisognano, O. Brüning, R. Calder, I. Collins, C. Fadley, W. Fawley, O. Gröbner, E. Gullikson, S. Heifets, N. Hilleret, D. Hunt, K. Kennedy, K.-J. Kim, K. Ohmi, J. Peterson, R. Rimmer, J. Rogers, F. Ruggiero, T. Stevens, W. Stoeffl, W. Turner, K. Yokoya, A. Zholents, F. Zimmermann, M. Zisman and M. Zolotorev. We are grateful to NERSC for supercomputer support.

References

[1] M. Izawa, Y. Sato and T. Toyomasu, "The Vertical Instability in a Positron Bunched Beam," Phys. Rev. Lett. **74**(25) (1995), pp. 5044–5047.

[2] Contributions by J. Rogers, M. Izawa, F. Zimmermann and Z. Y. Guo, these proceedings.

[3] K. Ohmi, "Beam Photo-Electron Interactions in Positron Storage Rings," Phys. Rev. Lett. **75**(8), pp. 1526–1529 (1995).

[4] "PEP-II: An Asymmetric B Factory–Conceptual Design Report," June 1993, LBL-PUB-5379/SLAC-418/CALT-68-1869/UCRL-ID-114055/UC-IIRPA-93-01.

[5] M. A. Furman and G. R. Lambertson, "The Electron-Cloud Instability in PEP-II: an Update," LBNL-40256/CBP Note-224/PEP-II AP note 97.07, to be published in the Proc. PAC97, Vancouver, BC, May 12–16, 1997.

[6] R. Kirby and F. King, private communication.

[7] W. Barry, J. Byrd, J. Corlett, M. Fahmie, J. Johnson, G. Lambertson, M. Nyman, J. Fox and D. Teytelman, "Design of the PEP-II transverse coupled-bunch feedback system," Proc. PAC95, Dallas, Texas, May 1995, p. 2681.

[8] P. M. Morse and H. Feschbach, *Methods of Theoretical Physics*, McGraw-Hill, 1953, ch. 10.

[9] J. D. Jackson, *Classical Electrodynamics, 2nd. ed.*, J. Wiley & Sons, 1975.

[10] S. Heifets, "Study of an Instability of the PEP-II Positron Beam," Proc. *Intl. Workshop on Collective Effects and Impedance for B Factories (CEIBA95)*, Tsukuba, Japan, 12–17 June 1995, Y. H. Chin, ed., pp. 295–321.

[11] H. Bruining, *Physics and Applications of Secondary Electron Emission*, Pergamon Press, 1954.

[12] H. Seiler, "Secondary Electron Emission in the Scanning Electron Microscope," J. Appl. Phys. **54**(11), Nov. 1983, pp. R1–R18.

[13] P. A. Redhead, J. P. Hobson and E. V. Kornelsen, *The Physical Basis of Ultrahigh Vacuum*, Chapman and Hall, Ltd., 1968, ch. 4 (reprinted by the AIP in 1993 as part of the American Vacuum Society Classics series).

[14] *Handbook of Mathematical Functions*, M. Abramowitz and I. A. Stegun, Eds., Dover Publications Inc., 9th printing, 1970.

[15] M. A. Furman, "Compact Complex Expressions for the Electric Field of 2-D Elliptical Charge Distributions," Am. J. Phys. **62**(12), Dec. 1994, pp. 1134–1140.

[16] M. Bassetti and G. A. Erskine, "Closed Expression for the Electric Field of a Two-Dimensional Gaussian Charge," CERN-ISR-TH/80-06.

[17] J. S. Berg, "Energy Gain in an Electron Cloud During the Passage of a Bunch," LHC project note 97, 1 July 1997.

[18] R. W. Hockney and J. W. Eastwood, *Computer Simulation Using Particles*, Inst. of Physics Publishing, 1988.

[19] A. W. Chao, *Physics of Collective Beam Instabilities in High-Energy Accelerators*, John Wiley & Sons, Inc., 1993.

[20] M. A. Furman, "The Electron-Cloud Effect in the LHC," to be published.

[21] I. Collins, private communication.

Disclaimer